Acta Geologica Polonica, Vol. 70 (2020), No. 3, pp. 363–396
DOI: 10.24425/agp.2019.126463

Thermal history of the Carboniferous strata in the northern part of the Intra-Sudetic Basin (SW Poland): A combined Raman spectroscopy and organic petrography study

DARIUSZ BOTOR[1], TOMASZ TOBOŁA[1] and MARTA WALICZEK[1]

[1] *AGH University of Science and Technology, Faculty of Geology, Geophysics and Environmental Protection, 30-059 Kraków, al. Mickiewicza 30, Poland.*
E-mail: botor@agh.edu.pl

ABSTRACT:

Botor, D., Toboła, T. and Waliczek, M. 2020. Thermal history of the Carboniferous strata in the northern part of the Intra-Sudetic Basin (SW Poland): A combined Raman spectroscopy and organic petrography study. *Acta Geologica Polonica*, **70** (3), 363–396. Warszawa.

Raman spectroscopy and vitrinite reflectance measurements of dispersed organic matter from Carboniferous shales in boreholes in the northern part of the Intra-Sudetic Basin were used for thermal history reconstruction. Microscopic investigations have shown that the organic matter is dominated by the vitrinite maceral group. In analysed samples, organic matter shows a varied degree of thermal alteration determined by the mean random vitrinite reflectance (VR_o) ranging from 0.72% to 3.80%. Mean apparent maximum vitrinite reflectance (R'_{max}) values reached 4.98%. The full width at half maximum of D1 and G bands in Raman spectra are well-correlated with mean VR_o and R'_{max}. Thermal maturity in the boreholes shows a regular increase with depth. Geological data combined with Raman spectroscopy and mean vitrinite reflectance results indicate that the analysed Carboniferous strata reached maximum paleotemperatures from c. 110 to c. 265°C. The regional paleogeothermal gradient in the late Paleozoic was c. 80°C/km. The Variscan heating event presumably caused a major coalification process of organic matter. The Carboniferous–Permian magmatic activity must have contributed to high heat flow, adding to the effect of sedimentary burial on the thermal maturity.

Key words: Raman spectroscopy; Vitrinite reflectance; Dispersed organic matter; Coalification; Lower Silesia Coal District; Bohemian Massif.

INTRODUCTION

Thermal maturity of dispersed organic matter (OM) in fine-grained rocks (shales, siltstones, mudstones, etc.) is usually evaluated using the pyrolysis method (e.g., Rock-Eval) and/or an optical technique termed vitrinite reflectance analysis (e.g., Taylor *et al.* 1998). Although a variety of parameters can be used to assess maximum paleotemperatures, the most commonly applied is mean random vitrinite reflectance (VR_o; e.g., Suchý *et al.* 1997, 2007; Littke *et al.* 2012; Hartkopf-Fröder *et al.* 2015; Waliczek *et al.* 2019). The widespread use of vitrinite reflectance is based on the broad temperature range over which it is applicable (Hartkopf-Fröder *et al.* 2015). Reconstruction of the thermal maturity trend versus depth allows the paleogeothermal gradient at the time of maximum burial to be determined (e.g., Taylor *et al.* 1998). During burial, the OM progressively experiences heating and higher temperatures that result in the formation and coalescence of aromatic rings of carbon in vitrinite (Carr and Williamson 1990). These rings form sheets, which change the physical property of the vitrinite reflectance, causing more

light to be reflected. The vitrinite reflectance method requires that samples exhibit a high-quality polish to insure vitrinite is scratch and relief free (e.g., Taylor *et al.* 1998). This approach to quantifying the thermal maturity of organic matter in shale has limitations as this technique can be time-intensive and requires an experienced organic petrographer to interpret different types of kerogen, from which only vitrinite is to be measured (Lupoi *et al.* 2017). This can be a difficult undertaking in the case of low concentrations of dispersed organic matter, the presence of other types of OM (such as solid bitumen, graptolites, etc.) that have similar optical properties, vitrinite reflectance suppression, and the physical quality of the sample and its preparation (e.g., Taylor *et al.* 1998; Lupoi *et al.* 2017). Finally, interlaboratory studies to evaluate the reproducibility of VR_o measurements suggested the use of a common methodology to improve measurement accuracy, but these significant improvements are still required (Hackley *et al.* 2015).

Whereas, in last decade laser Raman microspectroscopy (term used as Raman spectroscopy thereafter) is being increasingly used to assess the thermal maturity of OM in rocks (e.g., Beyssac *et al.* 2002a, b, 2003a, b; Jehlička *et al.* 2003; Rahl *et al.* 2005; Aoya *et al.* 2010; Guedes *et al.* 2010; Kouketsu *et al.* 2014; Lünsdorf *et al.* 2014; Morga *et al.* 2015; Lünsdorf and Lünsdorf 2016; Lünsdorf 2016; Lupoi *et al.* 2017; Henry *et al.* 2018, 2019; Zhang and Li 2019). The novelty of Raman spectroscopy is that it is a non-destructive method that allows for rapid data acquisition with relatively fast interpretation, combining both optical microscopy and vibrational spectroscopy (e.g., Beyssac *et al.* 2002a, b, 2003a, b; Guedes *et al.* 2010; Lahfid *et al.* 2010; Kouketsu *et al.* 2014; Hinrichs *et al.* 2014; Wilkins *et al.* 2014, 2015; Lünsdorf 2016; Henry *et al.* 2018, 2019; Zhang and Li 2019). Advances in instrumentation and data processing have spurred increased applications, and the technique can be performed directly on standard petrographic thin sections or thick slides used for routine VR_o measurements or on bulk kerogen HF-HCl separate fractions. However, problems related to sample preparation, using laser parameters and the methodology of spectra deconvolution are still being widely discussed in the literature (e.g., Aoya *et al.* 2010; Lahfid *et al.* 2010; Kouketsu *et al.* 2014; Lünsdorf *et al.* 2014; Lünsdorf 2016; Lünsdorf and Lünsdorf 2016; Henry *et al.* 2018, 2019). Laser Raman spectroscopy has the ability to be used alongside other petrological parameters such as VR_o, spore colouration index (SCI), fluorescence spectroscopy and Rock-Eval pyrolysis (T_{max}) in order to provide reliable assessment of the thermal maturity of organic matter. It can also be used as a cheap and rapid means to screen samples before conducting more expensive and time-consuming destructive analyses.

This study focuses on the use of Raman spectroscopy as a tool for evaluating correlations between Raman spectral data and thermal maturity expressed by VR_o in shale samples from the Intra-Sudetic Basin in SW Poland. Therefore, it allows for the reconstruction of the thermal history of analysed rocks. The thermal history of the Sudetes, NE Bohemian Massif (Text-fig. 1), is still a matter of debate, particularly due to the poorly preserved post-Variscan sedimentary record (e.g., Maluski *et al.* 1995; Migoń and Danišík 2012; Danišík *et al.* 2012; Sobczyk *et al.* 2015; 2019; Botor *et al.* 2017a, b, 2019). Particularly, in the Intra-Sudetic Basin (ISB) magmatic bodies are widely known (e.g., Awdankiewicz *et al.* 1999a, b 2004; Ulrych *et al.* 2011) and these represent a possible source of heat that could have directly influenced the thermal maturity of organic matter (e.g., Kwiecińska *et al.* 1992; Adamczyk *et al.* 2018). The aim of this study is to improve understanding of the thermal evolution of the Carboniferous strata in ISB. Diagenetic to very low metamorphic information revealed by the Raman spectroscopy and microscopic study of dispersed organic matter supplements the stratigraphic evidence and allows for new insight on the geological evolution during the coalification process.

GEOLOGICAL SETTING

The ISB is a large, 70 km long and 35 km wide, Variscan intramontane trough located at the NE margin of the Bohemian Massif (Text-fig. 1; e.g., Dziedzic 1971; Dziedzic and Teisseyre 1990; Awdankiewicz 1999a; Ulrych *et al.* 2006; Opluštil and Cleal 2007; Mazur *et al.* 2006, 2007). The total thickness of the basin fill reaches c. 12 km. The basin is framed by various crystalline basement units of Variscan consolidation age and by another Palaeozoic sedimentary basins (Text-figs 1, 2; e.g., Mazur *et al.* 2006, 2007).

Development of the ISB was initiated in the mid-Viséan (Turnau *et al.* 2005) as an intramontane depression bounded by tectonically active margins (Teisseyre 1968). The early Carboniferous fluvial sequence of the ISB starts with middle Viséan clastic sediments (Turnau *et al.* 2005) that are mainly composed of coarse-grained conglomerates and sedimentary breccias (Text-fig. 2; Teisseyre 1975). They are succeeded by upper Viséan (Turnau *et al.* 2005) fluvial sediments and late Viséan deposits of a marine

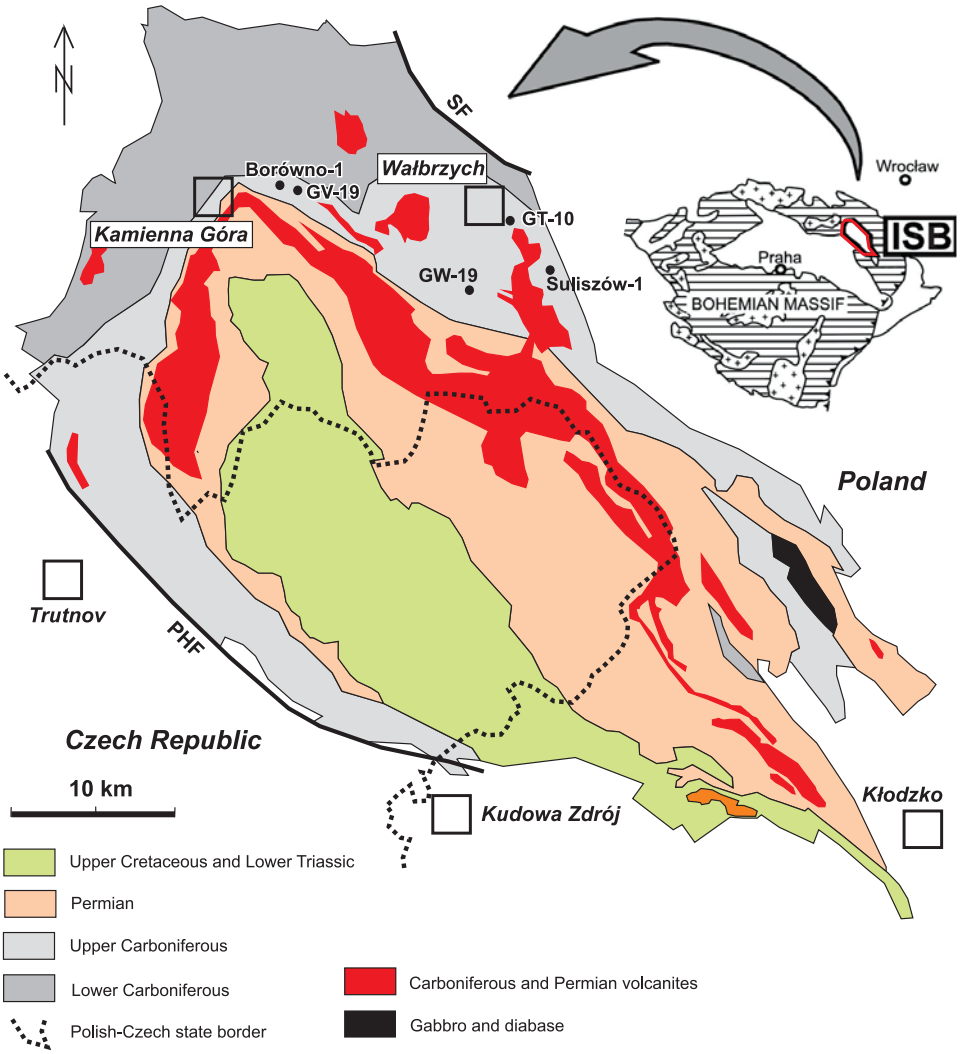

Text-fig. 1. Geological simplified map of the Intra-Sudetic Basin with location of analysed boreholes (modified after Grocholski and Augustyniak 1971; Sawicki 1995; Bossowski and Ihnatowicz 2006). SF – Struga Fault; PHF – Pořiči-Hronov Fault. Study area (red rectangular) is also shown on the sketch map of the Bohemian Massif (after Franke 1989).

transgression (Text-fig. 2; Żakowa 1963; Teisseyre 1968, 1975). Tectonic uplift at the transition from the early to late Carboniferous led to marine regression and the accumulation of an upper Carboniferous predominantly coal-bearing continental succession, occurring in the Polish and Czech part of the ISB (Text-fig. 2; Dziedzic 1970, 1971; Dziedzic and Teisseyre 1990; Bossowski and Ihnatowicz 1994; Opluštil *et al.* 2016; Pešek and Sivek 2016), that is well-known from bituminous and anthracite coal deposits (Kwiecińska 1967; Mastalerz and Jones 1988; Mastalerz and Smyth 1988; Mastalerz and Wilks 1992; Nowak 1993, 1996, 1997a, b 2000; Bossowski and Ihnatowicz 2006; Opluštil *et al.* 2016; Pešek and Sivek 2016).

The Autunian (lower Permian) sediments of the ISB comprise clastic deposits of alluvial fan, fluvial and lacustrine environments (Text-fig. 2; Dziedzic and Teisseyre 1990). Early Permian tectonic inversion caused significant exhumation of the elevated margins of the ISB (Dziedzic and Teisseyre 1990; Awdankiewicz 2004). In post-Variscan times, the basin fill succession was overlain by thin uppermost Zechstein to Lower Triassic continental sediments (Lorenz and Mroczkowski 1978) and a 1 km sequence of Upper Cretaceous shallow marine deposits (Text-fig. 2; Skoček and Valečka 1983; Uličný 2001; Uličný *et al.* 2009; Wojewoda *et al.* 2016). Because the Bohemian Massif formed a large and coherent

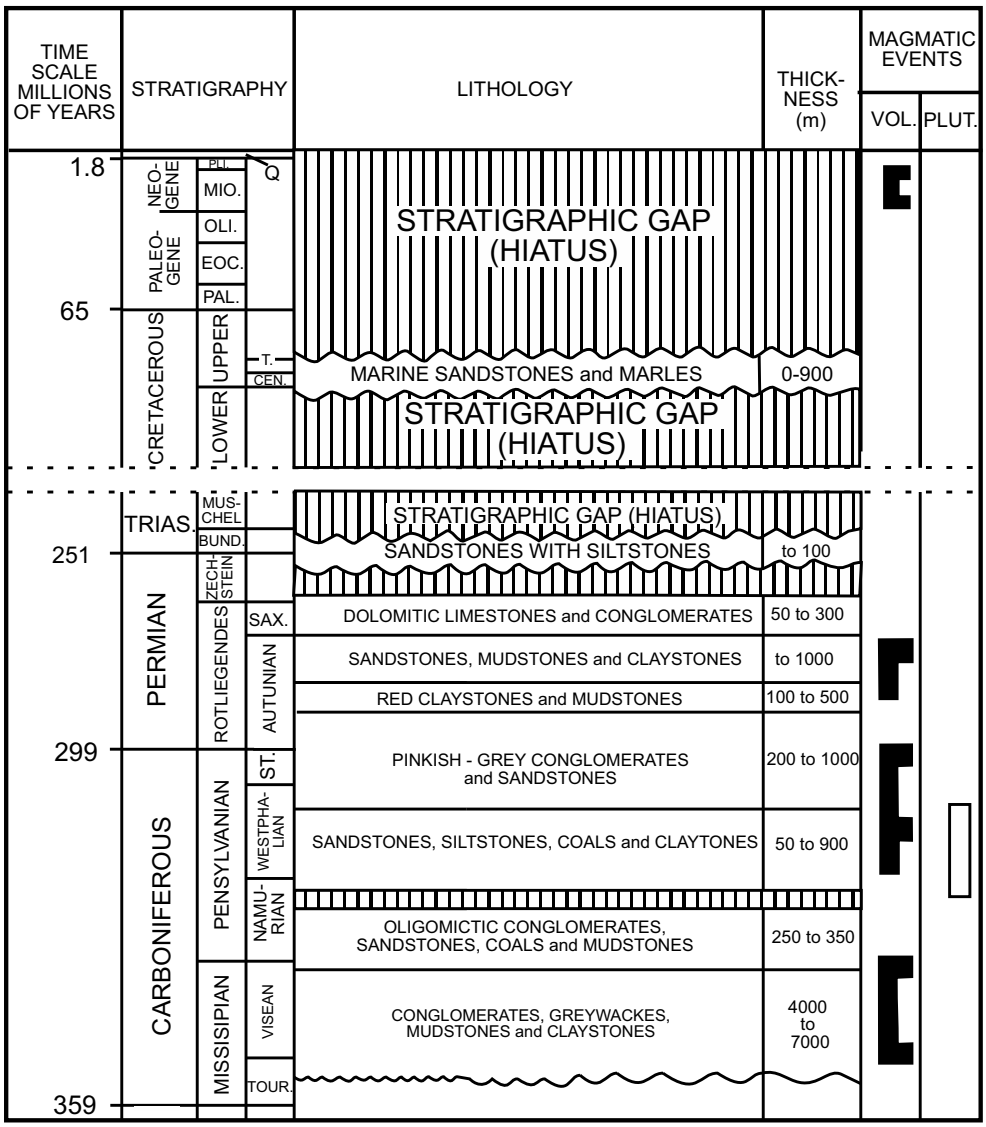

Text-fig. 2. Lithostratigraphy of the Intra-Sudetic Basin (based on Dziedzic 1971; Grocholski and Augustyniak 1971; Dziedzic and Teisseyre 1990; Awdankiewicz 1999a; Bossowski and Ihnatowicz 2006).

structural high between the Middle Triassic and the Middle Jurassic (Ziegler and Dèzes 2007) no sediments of Middle Triassic to Early Cretaceous age are known in the ISB. In the latest Cretaceous to Paleocene, the Bohemian Massif was influenced by transpressional deformation induced by far-field stresses from the Europe-Africa plate convergence (Kley and Voigt 2008). This led to reactivation of the Variscan basement faults (Scheck *et al.* 2002), the development of thrust-related uplift, exhumation of elevated basement blocks, and inversion of the Cretaceous basin (Kley and Voigt, 2008). These processes are evidenced by deformation of the Cretaceous strata, the abrupt cessation of sedimentation in the Late Cretaceous, and also by a distinct cooling phase recorded by thermochronological data (Skoček and Valečka 1983; Jarmołowicz-Szulc 1984; Ziegler 1987; Uličný 2001; Aramowicz *et al.* 2006; Ventura *et al.* 2009; Jarmołowicz-Szulc *et al.* 2009; Sobczyk *et al.* 2015; 2019; Botor *et al.* 2019). Subsequently, the Sudetes were eroded, resulting in the development of a peneplain (Migoń and Lidmar-Bergström 2001). In Cainozoic, basaltic volcanism penetrated the Sudetes (Birkenmajer *et al.* 2004;

Ulrych *et al.* 2011). Neogene uplift and deformation of the Bohemian Massif are attributed to lithospheric buckling and transpressional reactivation of crustal discontinuities (Ziegler *et al.* 2002; Ziegler and Dèzes 2007).

The Carboniferous and Permian geological evolution of the ISB was associated with three Variscan stages of volcanic/magmatic activity (Text-fig. 2). These occurred during the middle Viséan, the late Carboniferous, and the early Permian, the latter corresponding to a maximum of volcanic activity (Awdankiewicz *et al.* 1999a, b, 2004; Ulrych *et al.* 2011; Opluštil *et al.* 2016). The late Palaeozoic magmatism included widespread volcanic complexes of lavas, shallow-level intrusions, and volcaniclastic deposits interstratified in Permian and Carboniferous sedimentary successions (Awdankiewicz 1999a, 2004; Mazur *et al.* 2006, 2007).

Paleogeothermal gradients during metamorphism of the Variscides reached at least 40–60°C/km near subvolcanic intrusions, where coal was locally formed (Teichmüller and Teichmüller 1986). However, the intense heat generation by Variscan intrusions increased this value locally up to 90°C/km in the ISB (Kułakowski 1979). The upper Carboniferous, coal-bearing sequence of the ISB includes coals ranging from high-volatile bituminous to anthracitic rank (Kwiecińska 1967; Mastalerz and Jones 1988; Kwiecińska *et al.* 1992; Kwiecińska and Nowak 1997; Bossowski and Ihnatowicz 2006; Nowak 1993, 1996, 2000). The lowest values of vitrinite reflectance are recorded around the basin margins (c. 0.6% mean VR_o), while the highest ones appear in the centre (exceeding 4% R'_{max}). Average VR_o gradients are from c. 0.15 to 0.30% per 100 m, and locally reaching very high values (up to 0.60% per 100 m) in the centre of the basin (Mastalerz and Jones 1988; Nowak 2000). The most intense coalification presumably took place during the early Westphalian at temperatures of at least c. 160–170°C, with a paleogeothermal gradient of 80–100°C/km (Kułakowski 1979; Mastalerz and Jones 1988). The maximum temperature could be even higher in the areas of high R'_{max} values, particularly at the contact with intrusions and sills (e.g., Mastalerz and Jones 1988; Kwiecińska *et al.* 1992).

SAMPLES AND METHODS

The eighteen Carboniferous siltstone core samples were collected from five boreholes within the ISB. The samples contain only dispersed OM. No samples from coal seams were available. The rock samples were cut perpendicular to the bedding and from these rock pieces standard polished slides were prepared for vitrinite reflectance measurements (R'_{max} – mean apparent maximum reflectance, R'_{min} – mean apparent minimum reflectance and VR_o – mean random vitrinite reflectance) and laser Raman spectroscopy. In the case of the highly disordered low-grade OM which occurs within the diagenetic zone such type of sample can be used efficiently (Rahl *et al.* 2005; Kouketsu *et al.* 2014; Wilkins *et al.* 2014, 2015; Lünsdorf 2016; Botor *et al.* 2017a; Henry *et al.* 2019; Zhang and Li 2019). However, in high-ordered OM (particularly in graphite) several authors have shown that the polishing of a sample could cause a change in the Raman record (e.g., Katagiri *et al.* 1988; Wopenka and Pasteris 1993). Also Beyssac *et al.* (2003a) showed that in poorly organised OM, there is no significant difference, whereas in well-organised OM the spectra measured at the surface exhibit a higher contribution of the defect bands (D1 and D2). According to Lünsdorf (2016), in the VR_o measuring range of 1.0 to 7.0%, the Raman spectra are unaffected by polishing, if no final polishing below 1 μm is used. Therefore, no polishing less than 1 μm was used in this study. In a final step, only 1 μm monocrystalline diamond slurry was used. Further discussion of sample preparation method is given in Lünsdorf (2016). Raman spectra in all the samples in the present study consist of poorly organised OM, because thermal maturity of Carboniferous strata in ISB is generally much lower than graphite (e.g., Mastalerz and Jones 1988; Nowak 1993, 1996, 2000). Therefore, polished rock slides were used.

Microscopic study

The petrological investigations were performed using the Carl Zeiss Axio Imager A1m microscope equipped with photometer PMT, computer with PMT III software and HBO lamp. The vitrinite reflectance measurements were carried out in oil immersion (refractive index n = 1.518), 546 nm peak transmittance filter at a temperature of about 23°C in non-polarized light to obtain mean random vitrinite reflectance values (VR_o) and in polarized light during microscope stage rotation to get mean apparent maximum and minimum vitrinite reflectance values (R'_{max} and R'_{min}). Mineral standards of known reflectance were used for calibration: spinel (0.429%), yttrium-aluminium-garnet (0.905%), gadolinium-gallium-garnet (1.728%), and cubic zirconia (3.06%). Petrographic classification of dispersed OM in analysed samples was performed according to findings of ICCP

System 1994 (1998, 2001; Pickel *et al.* 2017), TSOP, and ICCP (Stasiuk *et al.* 2002). Photomicrographs of OM were taken using AxioCam MRc5 Zeiss camera. The applied microscopical investigations closely followed the guidelines published by Taylor *et al.* (1998), Pusz *et al.* (2014) as well as Hackley *et al.* (2015), and ASTM (2011). However, we prefer ASTM (2011) which is applied to reflectance of vitrinite dispersed in sedimentary rocks not only coals.

VR_o was used as an input parameter for the estimation of maximum palaeotemperature after Barker and Pawlewicz (1994) as well as Sweeney and Burnham (1990). In the present study, the formula Temperature 1 = ($\ln VR_o$ + 1.68)/0.0124 for the burial heating model and Temperature 2 = ($\ln VR_o$ + 1.19)/0.00782 for the hydrothermal heating model after Barker and Pawlewicz (1994) was used. The formulas are calibrated up to 7% VR_o (Barker and Pawlewicz 1994), whereas Sweeney and Burnham (1990) Easy%VR_o method is calibrated up to 4.6%VR_o.

Raman spectroscopy

In the past few decades, the development of optics (including lasers) and computing has influenced progress in the Raman spectroscopy technique which allows for detailed study of OM and their thermal transformation (e.g., Beyssac *et al.* 2002a, b, 2003a, b; Jehlička *et al.* 2003; Rahl *et al.* 2005; Aoya *et al.* 2010; Kouketsu *et al.* 2014; Lünsdorf *et al.* 2014; Lünsdorf 2016; Wilkins *et al.* 2014, 2015; Botor *et al.* 2017a; Henry *et al.* 2018, 2019; Zhang and Li 2019). The Raman spectrum of OM is composed of first-order (1000–1800 cm^{-1}) and second-order (2500–3350 cm^{-1}) regions (e.g., Pasteris and Wopenka 1991; Beyssac *et al.* 2002a). The first-order range is more intensive and informative (Text-fig. 3). Within this range the line-shape of the Raman spectrum changes with increasing order of the OM, which increases with the coalification and degree of metamorphism, caused mainly by temperature increase (Text-fig. 3; e.g., Wopenka and Pasteris 1993; Beyssac et al. 2002a, b, 2003a, b; Morga 2011, 2014; Lahfid *et al.* 2010; Henry *et al.* 2018, 2019; Zhang and Li 2019).

Raman spectroscopy is often used to characterize the ordering degree of OM in various geological settings. Generally, in the diagenetic to early metamorphic range, at least five Raman bands in the first-order spectrum of OM (Text-fig. 3) are usually visible (e.g., Lünsdorf *et al.* 2014; Kouketsu *et al.* 2014). These bands are denominated as D1 (c. 1350 cm^{-1}), D2 (c. 1620 cm^{-1}), D3 (c. 1500 cm^{-1}), D4 (c. 1250 cm^{-1}) and G (c. 1580 cm^{-1}). The G band is an indicator of the

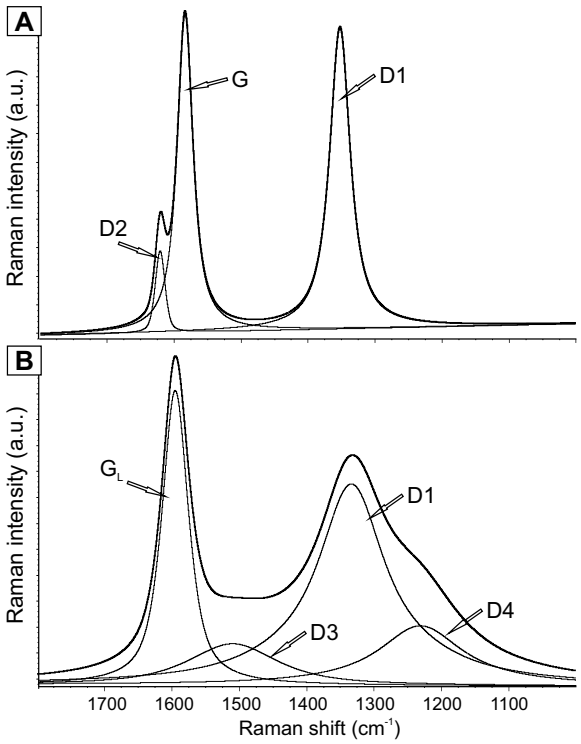

Text-fig. 3. Examples of Raman spectra of organic matter (modified after Toboła 2018). A – High-ordered organic matter (> c. 300°C). B – Low-ordered organic matter (< c. 300°C).

hexagonal graphite lattice (Tuinstra and Koenig 1970; Reich and Thomsen 2004; Ferrari and Robertson 2007). The bands marked by the letter "D" are considered as defect-induced bands and refer to disordered crystal structure or the presence of crystal defects (Beny-Bassez and Rouzaud 1985; Aoya *et al.* 2010; Pimenta *et al.* 2007). The origin and vibrational mode of these bands is debatable and several plausible interpretations have been proposed (Tuinstra and Koenig 1970; Beny-Bassez and Rouzaud 1985; Pócsik *et al.* 1998; Matthews *et al.* 1999; Beyssac *et al.* 2003a, b; Reich and Thomsen 2004; Sadezky *et al.* 2005; Pimenta *et al.* 2007; Potgieter-Vermaak *et al.* 2011; Ulyanova *et al.* 2014; Henry *et al.* 2018, 2019).

In a diagenetic regime, an increase in temperature during burial causes loss of hydrogen, oxygen, nitrogen, and other components in OM (e.g., Kouketsu *et al.* 2014). At the same time, carbon atoms become progressively organized, finally into a graphite-like structure (Beyssac *et al.* 2003a, b). In the low ordered OM the G and D2 bands are not separated and they form one band GL around 1600 cm^{-1} (e.g., Rahl *et al.* 2005; Lahfid *et al.* 2010; Lünsdorf *et al.*

2014; Kouketsu *et al.* 2014). Therefore, in this paper G band actually refers to GL *sensu* Kouketsu et al. (2014), then it is used in this way thereafter. The D1 band is very wide and its intensity is lower than the G band. The D3 and D4 bands are clearly visible in the low ordered OM (Rahl *et al.* 2005; Aoya *et al.* 2010; Kouketsu *et al.* 2014; Lünsdorf *et al.* 2014).

With an increase of OM order, the D3 and D4 bands disappear gradually and the D1 band becomes narrower. Simultaneously, the G and D2 bands become distinguishable (Text-fig. 3). Further transformations with increase of temperature result in the disappearance of the D1 and D2 bands. Therefore, in pure graphite, only the G band occurs (Tuinstra and Koenig 1970; Nemanich and Solin 1979; Beyssac *et al.* 2002a; Reich and Thomsen 2004; Ferrari and Robertson 2007; Kouketsu *et al.* 2014).

Based on changes observed in the line shapes of Raman spectra and their decomposition, several attempts have been made to determine the temperature of OM transformations. The first approach of temperature estimation from the decomposition of Raman spectra was made by Beyssac *et al.* (2002a). They notice that the R2 ratio calculated from the equation R2 = D1/(G+D1+D2), where D1, D2 and G are decomposed peaks area, increases linearly with grade of metamorphism. Such a geothermometer is valid for regional metamorphism in the temperature range c. 330–650°C (Beyssac *et al.* 2002a). On the basis of the Beyssac *et al.* (2002a) R2 ratio, Aoya *et al.* (2010) extended the geothermometer to contact metamorphic rocks. The application of Raman spectroscopy of OM (RSOM) for low-temperature (c. 100–300°C) transformation of rocks was performed by Rahl *et al.* (2005). These authors used two ratios i.e. R2 and R1 = D1/G (bands height) for temperature estimation. Another methodology of RSOM for low-temperature (c. 200–320°C) transformation was applied by Lahfid *et al.* (2010). Then Kouketsu *et al.* (2014) presented a different approach to the problem of low-temperature estimation, and proposed a fitting procedure applicable over a wide range of temperatures (c. 150–650°C). According to the metamorphic grade of OM, the procedure of peak fitting was shared into seven parts and for each part, they proposed a different procedure of peak fitting. The geothermometer described by Kouketsu *et al.* (2014) is generally based on the full width at half maximum (FWHM) of decomposed peaks. For maximum temperature transformation, Kouketsu *et al.* (2014) used two equations. The first was based on FWHM of the D1 band and the second based on FWMH of the GL band.

Experimental procedures

The Raman analyses of OM were performed on the same samples as in the petrographical part of this study. A Thermo Scientific DXR^{TM} spectrometer (installed at AGH in Kraków) with a 532 nm Nd-YAG laser was used to obtain the Raman spectra. The spectrometer was equipped with an Olympus, BX51 confocal microscope with 10×, 50× and 100× objectives. The laser power on the sample surface was set at 0.5 mW. The scattered light was collected by backscattered geometry with a 25 μm pinhole and a holographic notch filter and finally dispersed using a 900 lines/mm grating and analysed by a cooled CCD detector of 256 × 1024 pixels. Spatial resolution was about 1 μm and wave number resolution c. 1 cm^{-1}. The acquisition time was 30 s (assumed as a minimum time to obtain reliable results: Kouketsu *et al.* 2014). The Raman system was calibrated against the 520.4 cm^{-1} line of a Si-wafer. In each sample, over 30 different organic particles were measured. The Raman spectra were decomposed, using Omnic ver. 4.12 software (Thermo Fisher Scientific, Inc.) with a pseudo-Voigt function (Gaussian-Lorentzian Sum) and corrected for the fluorescence background by subtracting a linear baseline in the spectral range 1000–1800 cm^{-1}. The workflow of Kouketsu *et al.* (2014) and the methodological aspects of decomposition of the Raman spectra of OM highlighted by Aoya *et al.* (2010) and Lünsdorf *et al.* (2014) were taken into account. Maximum temperature OM transformation was calculated using Kouketsu *et al.* (2014) equations i.e.: T1 means temperature calculated based on FWHM of D1 band and T2 means temperature base on FWHM of GL band. Detailed discussion of the applied methodology is given by Botor *et al.* (2017a).

RESULTS

Microscopic data

Microscopic analysis of OM was carried out on eighteen samples of Carboniferous shales from ISB. Samples were taken from five wells: Borówno-1 (3 samples), GV-19 (5 samples), GW-19 (3 samples), GT-10 (5 samples), and Suliszów (2 samples). The measurement of reflectance of vitrinite was presented in the form of measurements of the mean random vitrinite reflectance (VR_o) and as well as mean apparent maximum (R'_{max}) and mean apparent minimum (R'_{min}) measurements of vitrinite reflectance. The results of microscopic analyses are presented in four

Well	Sample	Depth (m)	VR_o (%)	N	SD	VR_o (%) range
Borówno-1	4s	162.2	0.72	59	0.05	0.65–0.80
	12s	660.8	0.88	103	0.04	0.80–0.97
	9s	850.0	1.08	102	0.06	0.94–1.19
Suliszów	7s	621.6	1.65	96	0.07	1.50–1.77
	5s	667.0	1.84	80	0.05	1.74–1.94
GV-19	8s	403.5	0.92	27	0.05	0.79–1.00
	21s	403.9	0.91	82	0,04	0.80–0.99
	15s	819.2	1.37/1.26*/1.45**	76	0.05	1.30–1.47
	3s	840.1	1.16	71	0.09	0.97–1.37
	11s	985.7	1.34	46	0.06	1.22–1.47
GW-19	2s	1912.5	2.73	41	0.10	2.57–2.92
	1s	1918.8	3.80	79	0.10	3.51–3.95
	17s	1924.4	3.80	111	0.12	3.54–4.00
GT-10	10s	821.3	1.50	73	0.06	1.33–1.55
	13s	848.8	1.53	114	0.07	1.34–1.63
	6s	948.0	1.65	86	0.05	1.53–1.78
	20s	1048.0	1.72	113	0.09	1.49–1.92
	22s	1098.0	2.18	98	0.06	2.03–2.29

Table 1. Mean random vitrinite reflectance data for the shale samples from the Intra-Sudetic Basin. Explanations: VR_o – mean random vitrinite reflectance; N – number of measurements; SD – standard deviation. In the sample 15s, two vitrinite population were found. VR_o = 1.37% is the mean reflectance values for two populations of vitrinite. The N, SD. and VR_o range values in Table 1 are presented for two populations of vitrinite. The first vitrinite population is characterized by VR_o* = 1.26%, N = 40, SD = 0.05 and the range of VR_o* values between 1.17 and 1.34%. The second vitrinite population is characterized by VR_o** = 1.45%, N = 49, SD = 0.06 and the range of VR_o** values between 1.34 and 1.53%.

tables (Tables 1–4) and in seven figures (Text-figs 4–10). Organic matter in the analysed samples is represented mainly by macerals from the vitrinite group (collotelinite) and to a lesser extent by macerals from the inertinite group with semifusinite the most frequently occurred macerals (Text-figs 4 and 5).

The exception is made in the samples from the Borówno-1 borehole, in which the presence of macerals from the inertinite and liptinite groups has increased compared to the remaining samples. Liptinite macerals are present in the form of cutinite and sporinite. In the samples from the GV-19 well from a depth of about 400 m (samples 8s and 21s) trace amount of liptinite macerals was observed. In the remaining samples, there is too high a degree of thermal alteration of organic matter, and macerals from the liptinite group are unrecognizable in blue light (Taylor *et al.* 1998; Pickel *et al.* 2017). In three samples from the GV-19 (15s, 3s, 11s) well, organic matter occurs in the form of small fragments (>10 μm) of both inertinite and vitrinite macerals. In these samples, fragments of semifusinite similar to vitrinite, and showing VR_o properties similar to vitrinite, often appear. In one of the samples from the GV-19 (15s) well, two vitrinite populations were observed (Text-fig. 6).

The vitrinite population with a higher degree of thermal transformation is present at the "margins" of the 15s sample. For the samples in which the highest VR_o were measured (samples 1s, 17s), the presence of structurally modified vitrinite was also noticed. In addition to the homogeneous vitrinite laminates, crumbled, often shredded laminate fragments (Text-fig. 5A) and dispersed particles of vitrinite occur.

Dispersed organic matter in the samples analysed shows a varied degree of thermal alteration determined by the mean VR_o index ranging from 0.72 to 3.80% (Table 1). The number of measurements varies from 27 to 117, usually above 50. The values of standard deviations are from 0.04 to 0.12. The lowest thermal maturated organic matter occurs in samples from the Borówno-1 borehole (0.72–1.08%VR_o). A similar degree of transformation of organic matter (0.92% VR_o) was measured for 2 samples from borehole (GV-19). The highest degree of thermal alteration of organic matter expressed by the mean VR_o was measured for samples from the GW-19 well, which are in the range from 2.73 to 3.80%. At a depth of 1912.5 m, the VR_o value is 2.73%, while in the samples taken 6 and 12 m deeper a significant jump in degree of coalification was observed with VR_o values 3.80%. Unfortunately, no lithological information is available for this sampled interval that could suggest heating by magmatic rocks. However, most of the analysed samples show a range of values from c. 1.30 to c. 2.00% (Table 1).

Vitrinite reflectance anisotropy (bireflectance, $VR_b = R'_{max} - R'_{min}$) was assessed in samples having mean random VR_o above 1.0%, because below this value anisotropy is very low and does not have

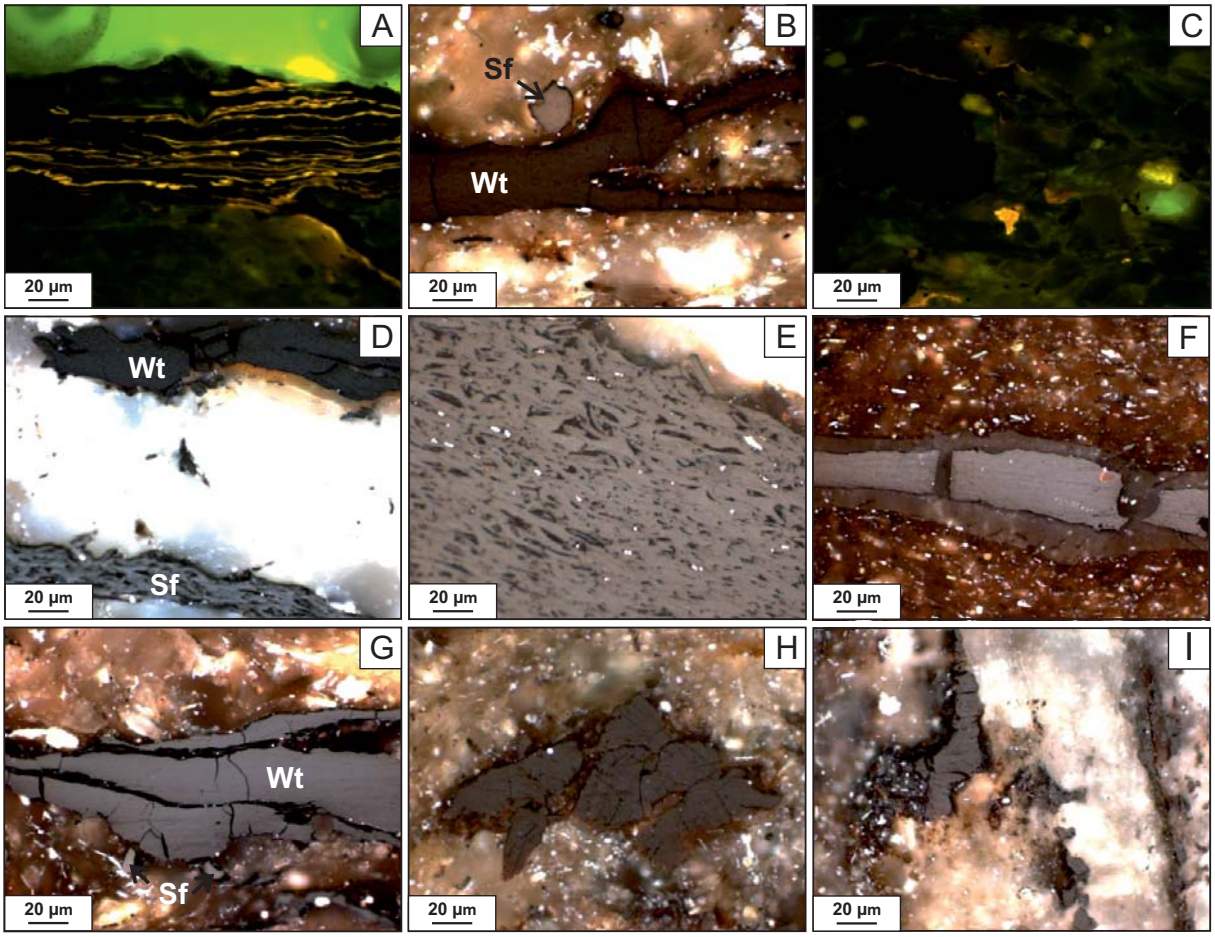

Text-fig. 4. Photomicrographs of organic matter from the Intra-Sudetic Basin. A – Orange fluorescing cutinite, sample 4s, borehole Borówno-1. B – Laminae of vitrinite (Wt), and small semifusinite (Sf) fragment, sample 4s borehole Borówno-1. C – Orange fluorescing sporinite, sample 4s, borehole Borówno-1. D – Vitrinite (Wt) and semifusinite (Sf), sample 9s, borehole Borówno-1. E – Semifusinite, sample 9s, borehole Borówno-1. F – Vitrinite, sample 21s, borehole GV-19; G – Vitrinite, sample 15s, borehole GV-19. H – Vitrinite, sample 21s, borehole GV-19. I – Vitrinite fragment, sample 15s borehole GV-19. A and C – blue light excitation, whereas B, D to I – reflected white light. All examination under oil immersion.

particular significance for thermal maturity assessment (Teichmüller 1982; Koch and Günther 1995; Taylor *et al.* 1998). However, the mean maximum reflectance measurement of vitrinite is recommended above 1.30% VR_o (ICCP, 1998). Measured R'_{max} values for analysed sample set are in the range from 1.10 to 4.98%, whereas the measured values of the R'_{min} are in the range from 0.90 to 2.70% (Table 2). Values R'_{min} standard deviations are from 0.03 to 0.39, whereas values for the R'_{max} standard deviations are from 0.04 to 0.24 (Table 2).

Histograms for the mean VR_o, R'_{max}, R'_{min}, for the majority of the samples analysed, are unimodal in character with low values of standard deviation and anisotropy (Text-figs 7 and 8). An exception are samples in which there is highly thermally transformed organic matter (2s; 1s; 17s). The higher values of standard deviation and anisotropy for these samples are most likely related to the phenomenon of increasing values with the thermal transformation (Houseknecht et al., 1993; ICCP 1998; Komorek and Morga 2002; Komorek and Morga 2007). However, the standard deviation of the vitrinite measurements of the analysed samples, even those with higher maturity, seems to be low.

Bruns and Littke (2015) concluded that the standard deviation of vitrinite reflectance measurements at high levels of thermal maturity depends on the lithology, and in coals it is generally smaller than in other sedimentary rocks such as claystone, sandstone,

Well	Sample	Depth (m)	VR_o (%)	R'_{max}(%)	N	SD	R'_{max}(%) range	R'_{min}(%)	N	SD	R'_{min}(%) range	VR_b(%)
Borówno-1	4s	162.2	0.72	–	–	–	–	–	–	–	–	–
	12s	660.8	0.88	–	–	–	–	–	–	–	–	–
	9s	850.0	1.08	1.10	44	0.05	1.03–1.20	0.90	44	0.03	0.83–0.96	0.20
Suliszów	7s	621.6	1.65	1.84	36	0.05	1.74–1.92	1.51	36	0.13	1.30–1.68	0.33
	5s	667.0	1.84	2.22	36	0.07	2.12–2.33	1.64	36	0.12	1.39–1.76	0.58
GV-19	8s	403.5	0.92	–	–	–	–	–	–	–	–	–
	21s	403.9	0.91	–	–	–	–	–	–	–	–	–
	15s	819.2	1.37/ 1.26*/ 1.45**	1.48/ 1.37*/ 1.59**	48	0.12	1.32–1.72	1.35/ 1.25*/ 1.44**	48	0.10	1.17–1.47	0.13/ 0.12*/ 0.15**
	3s	840.1	1.16	1.25	60	0.05	1.16–1.36	1.05	57	0.06	0.95–1.16	0.20
	11s	985.7	1.34	1.49	16	0.04	1.44–1.54	1.28	16	0.06	1.24–1.39	0.21
GW-19	2s	1912.5	2.73	2.80	32	0.17	2.59–3.13	1.66	32	0.20	1.39–1.97	1.14
	1s	1918.8	3.80	4.98	48	0.16	4.36–4.98	1.99	48	0.21	1.62–2.38	2.99
	17s	1924.4	3.80	4.84	57	0.24	4.45–5.24	2.70	52	0.39	2.26–3.58	2.14
GT-10	10s	821.3	1.50	1.53	40	0.04	1.46–1.60	1.29	40	0.06	1.17–1.40	0.24
	13s	848.8	1.53	1.56	44	0.04	1.51–1.63	1.34	44	0.06	1.26–1.45	0.22
	6s	948.0	1.65	1.76	40	0.07	1.62–1.84	1.40	40	0.10	1.20–1.60	0.36
	20s	1048.0	1.72	1.79	40	0.09	1.68–1.94	1.34	41	0.12	1.16–1.54	0.45
	22s	1098.0	2.18	2.36	46	0.10	2.20–2.46	2.02	44	0.07	1.80–2.22	0.34

Table 2. Vitrinite reflectance data of the R'_{max} and R'_{min}. Explanations: VR_o – mean random vitrinite reflectance; R'_{max} – mean apparent maximum vitrinite reflectance; R'_{min} – mean apparent minimum vitrinite reflectance; N – number of measurements; SD – standard deviation; VR_b – bireflectance $VR_b = R'_{max} – R'_{min}$. In the Table 2 the measurement statistics N; SD; R'_{max} range; R'_{min} range for a sample 15s were given without distinction into two populations of vitrinite. The first vitrinite population (*) is characterized by VR_o* = 1.26%. R'_{min}* = 1.25%; N = 24; SD = 0.05 with the range of R_{min} *values between 1.17 and 1.33% and R'_{max}* = 1.37%; N = 24; SD = 0.04 with the range of R'_{max}*values between 1.32 and 1.45%. The second vitrinite population is characterized by VR_o** = 1.45%; N = 49; SD = 0.06 and the range of VR_o** values between 1.34 and 1.53%. The second vitrinite population (**) is characterized by VR_o** = 1.45%. R'_{min}* = 1.44%; N = 24; SD = 0.02 with the range of R'_{min}** values between 1.41 and 1.47% and R'_{max}** = 1.59%; N = 24; SD = 0.06 with the range of R'_{max} **values between 1.53 and 1.72%.

S	VR_o	R'_{max}	R'_{min}	I	I'	II	II'	III	III'	IV	IV'	V	V'	VI	VI'	VII	VII'	VIII	VIII'	IX	IX'	X	X'	XI	XI'	XII	XII'
9s	1.08	1.1	0.9	1.03	0.07	1.15	0.05	1.15	0.05	1.17	0.07	1.15	0.05	1.15	0.05	1.15	0.05	1.24	0.14	1.16	0.06	1.13	0.03	1.01	0.09	1.22	0.12
7s	1.65	1.84	1.51	1.73	0.11	1.76	0.08	1.75	0.09	1.80	0.04	1.76	0.08	1.75	0.09	1.83	0.01	1.96	0.12	1.78	0.06	1.75	0.09	1.79	0.05	1.74	0.10
5s	1.84	2.22	1.64	2.03	0.19	1.96	0.26	1.95	0.27	2.01	0.21	1.96	0.26	1.96	0.26	2.06	0.16	2.20	0.02	1.98	0.24	1.95	0.27	2.05	0.17	1.94	0.28
15s	1.37	1.48	1.35	1.44	0.04	1.46	0.02	1.45	0.03	1.49	0.01	1.46	0.02	1.46	0.02	1.49	0.01	1.60	0.12	1.48	0.00	1.44	0.04	1.40	0.08	1.47	0.01
3s	1.16	1.25	1.05	1.18	0.07	1.24	0.01	1.23	0.02	1.26	0.01	1.23	0.02	1.23	0.02	1.24	0.01	1.34	0.09	1.25	0.00	1.21	0.04	1.12	0.13	1.29	0.04
11s	1.34	1.49	1.28	1.42	0.07	1.43	0.06	1.42	0.07	1.46	0.03	1.42	0.07	1.42	0.07	1.46	0.03	1.57	0.08	1.44	0.05	1.41	0.08	1.36	0.13	1.44	0.05
2s	2.73	2.8	1.66	2.42	0.38	2.91	0.11	2.90	0.10	3.00	0.20	2.91	0.11	2.90	0.10	3.13	0.33	3.33	0.53	2.94	0.14	2.92	0.12	3.26	0.46	3.08	0.28
1s	3.80	4.98	1.99	3.98	1.00	4.05	0.93	4.03	0.95	4.18	0.80	4.06	0.92	4.04	0.94	4.41	0.57	4.68	0.30	4.09	0.89	4.09	0.89	4.73	0.25	4.87	0.11
17s	3.80	4.84	2.7	4.13	0.71	4.05	0.79	4.03	0.81	4.18	0.66	4.06	0.78	4.04	0.80	4.41	0.43	4.68	0.16	4.09	0.75	4.09	0.75	4.73	0.11	4.87	0.03
10s	1.5	1.53	1.29	1.45	0.08	1.60	0.07	1.59	0.06	1.64	0.11	1.60	0.06	1.59	0.06	1.65	0.12	1.77	0.24	1.62	0.09	1.58	0.05	1.58	0.05	1.59	0.06
13s	1.53	1.56	1.34	1.49	0.07	1.63	0.07	1.62	0.06	1.67	0.11	1.63	0.07	1.63	0.07	1.69	0.13	1.81	0.25	1.65	0.09	1.62	0.06	1.62	0.06	1.62	0.06
6s	1.65	1.76	1.4	1.64	0.12	1.76	0.00	1.75	0.01	1.80	0.04	1.76	0.00	1.75	0.01	1.83	0.07	1.96	0.20	1.78	0.02	1.75	0.01	1.79	0.03	1.74	0.02
20s	1.72	1.79	1.34	1.64	0.15	1.83	0.04	1.82	0.03	1.88	0.09	1.83	0.04	1.83	0.04	1.91	0.12	2.05	0.26	1.85	0.06	1.82	0.03	1.88	0.09	1.81	0.02
22s	2.18	2.36	2.02	2.25	0.11	2.32	0.04	2.31	0.05	2.39	0.03	2.32	0.04	2.32	0.04	2.47	0.11	2.63	0.27	2.35	0.01	2.32	0.04	2.51	0.15	2.34	0.02

Table 3. The calculated mean R'_{max}. Explanations: S – sample; VR_o – mean measured vitrinite reflectance (%); R'_{max} – mean apparent measured maximum vitrinite reflectance. R'_{min} – mean apparent measured minimum vitrinite reflectance. Mean maximum vitrinite reflectance (R'_{max} equivalent) converted applying formulas: I – Hevia and Virgos (1977); II – Ting (1978); III – Hoover and Davis (1980); IV – Neavel et al. (1981); V – Diessel and McHugh (1986); VI – England and Bustin (1986); VII – Friedel et al. (1995); VIII – Koch and Gunther (1995); IX – Komorek and Pozzi (1996); X – Komorek and Morga (2002); XI – this study linear regression; XII – this study polynomial regression. $I' = \left| R'_{max} - I \right|$ – the module of difference between mean measured maximum vitrinite reflectance and converted mean maximum vitrinite reflectance determined for each of the formulas.

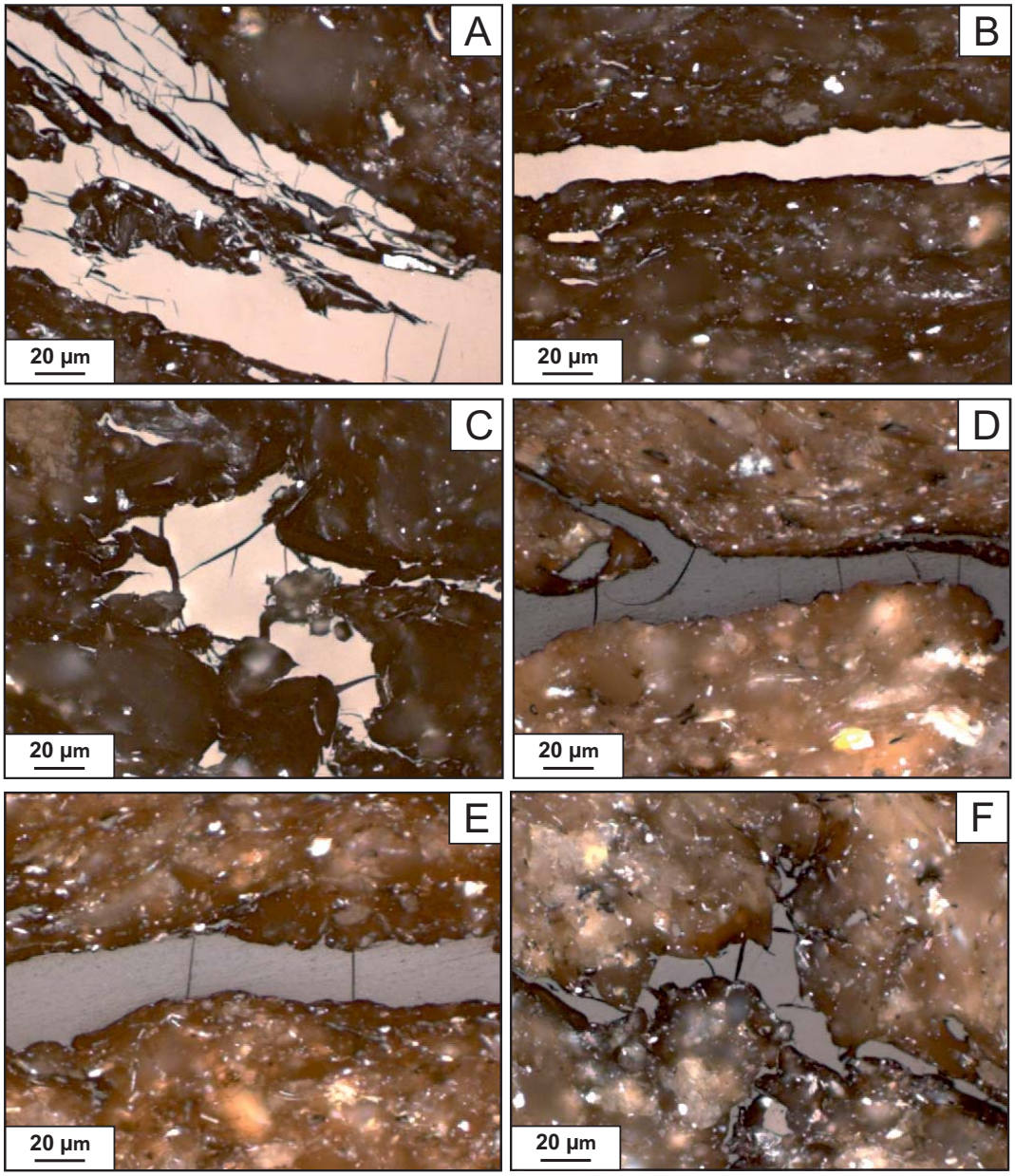

Text-fig. 5. Photomicrographs of vitrinite particles from the Intra-Sudetic Basin. A and B – Sample 1s, borehole GW-19. C – Sample 17s, borehole GW-19. D – Sample 10s, borehole GT-10. E – Sample 6s, borehole GT-10. F – Sample 22s, borehole GT-10. Photomicrographs under reflected white light and examination under oil immersion.

and siltstone. This may explain the low standard deviation for the analysed coaly shales at higher levels of thermal maturity. The scatterplot of the mean apparent maximum reflectance values R'_{max} against the average mean random reflectance values of the vitrinite VR_o points to a very strong linear relationship between the discussed parameters described by the Pearson linear correlation coefficient r = 0.99 and the determination coefficient r^2 = 0.98 (Text-fig. 9). However, an even better fit can be obtained for the polynomial regression. The bireflectance increases in range from 0.13 to 2.99% in a regular manner with depth and mean VR_o (Table 2). In most samples the bireflectance ranges from 0.13 to 0.58%, except the samples (from depth 1912.5–1924.4 m) from GW-19 well having 1.14 to 2.99 values (Table 2).

Calculated R'_{max} using different formulas are given in Table 3 and Text-fig. 10. The average difference

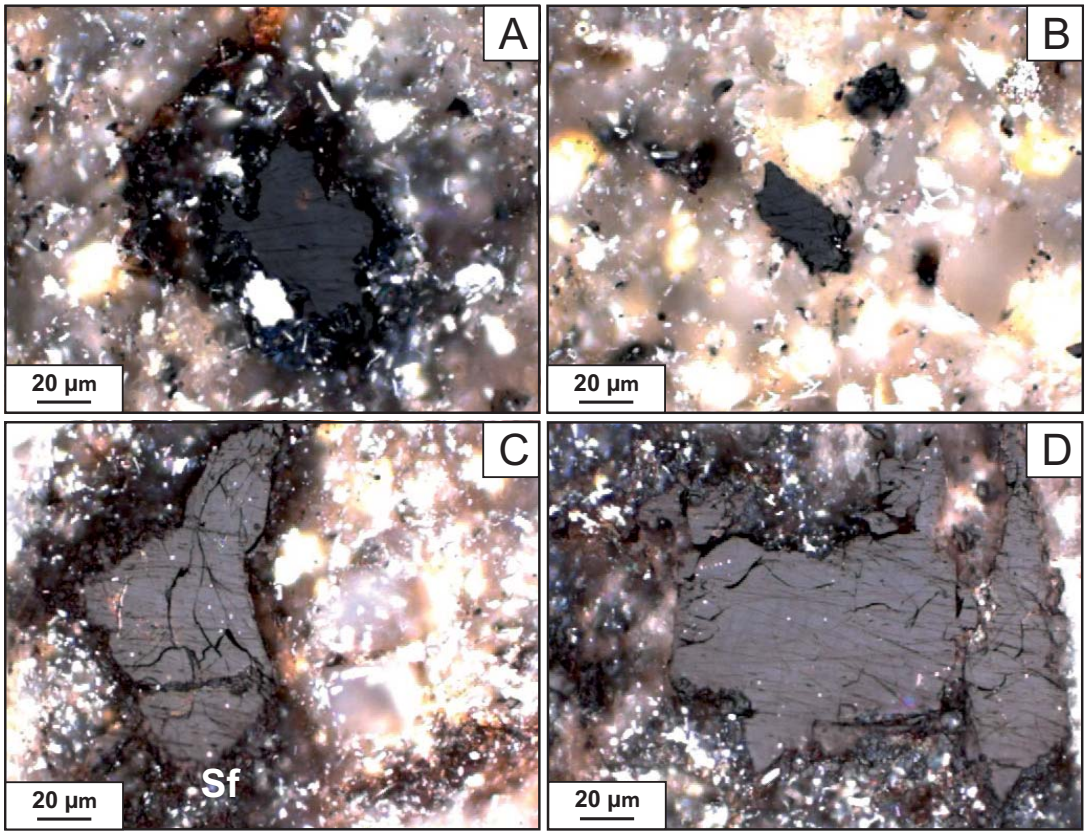

Text-fig. 6. Photomicrographs of two populations of vitrinite occurred in sample 15s from borehole GV-19. A and B – Lower reflecting population of vitrinite (VR_o = 1.26%). C and D – higher reflecting vitrinite (VR_o = 1.45%). Photomicrographs under reflected white light and examination under oil immersion.

I = R'_{max} equivalent = $(3VR_o - R'_{min})/2$ (Hevia and Virgos 1977)	$\sum \lvert R'_{max} - I \rvert = 0.215$
II = R'_{max} equivalent = $1.066*VR_o$ (Ting 1978)	$\sum \lvert R'_{max} - II \rvert = 0.175$
III = R'_{max} equivalent = $1.061*VR_o$ (Hoover and Davis 1980)	$\sum \lvert R'_{max} - III \rvert = 0.178$
IV = R'_{max} equivalent = $1.06*VR_o - 0.024$ (Neavel *et al.* 1981)	$\sum \lvert R'_{max} - IV \rvert = 0.167$
V = R'_{max} equivalent = $1.07*VR_o - 0.01$ (Diessel and McHugh 1986)	$\sum \lvert R'_{max} - V \rvert = 0.175$
VI = R'_{max} equivalent = $(VR_o - 0.0011)/0.94$ (England and Bustin 1986)	$\sum \lvert R'_{max} - VI \rvert = 0.177$
VII = R'_{max} equivalent = $1.2*VR_o - 1.50$ (Friedel *et al.* 1995)	$\sum \lvert R'_{max} - VII \rvert = 0.152$
VIII = R'_{max} equivalent = $1.2672*VR_o - 0.1318$ (Koch and Gunther 1995)	$\sum \lvert R'_{max} - VIII \rvert = 0.202$
IX = R'_{max} equivalent = $1.077*VR_o$ (Komorek and Pozzi 1996)	$\sum \lvert R'_{max} - IX \rvert = 0.170$
X = R'_{max} equivalent = $1.09*VR_o - 0.052$ (Komorek and Morga 2002)	$\sum \lvert R'_{max} - X \rvert = 0.173$
XI = R'_{max} equivalent = $1.3684*VR_o - 0.4708$ (this study I)	$\sum \lvert R'_{max} - XI \rvert = 0.137$
XII = R'_{max} equivalent = $0.5895 + 0.3702*VR_o + 0.199*(VR_o)^2$ (this study II)	$\sum \lvert R'_{max} - XII \rvert = 0.09$

Table 4. The equations used for calculation R'_{max} and average difference modules between mean measured maximum vitrinite reflectance and converted mean maximum vitrinite reflectance determined for each of the formulas. Explanations: $\sum \lvert R'_{max} - I \rvert = 0.215$ – the average difference modules between mean measured maximum vitrinite reflectance and converted mean maximum vitrinite reflectance determined for each of the formulas.

modules between mean apparent maximum vitrinite reflectance R'_{max} and converted mean maximum vitrinite reflectance R'_{max}-equivalent determined using published formulas are presented in Table 4. The smallest differences between these parameters are obtained for the polynomial formula presented in this study. Good results are observed for equations XI, VII, and IV (Table 3, Text-fig. 10). The published formulas presented in Tables 3 and 4 are linear regressions and were mostly valid up to about 2.0% R'_{max}. The relationship between VR_o and R'_{max} at higher coalification is not linear (Koch and Günther 1995).

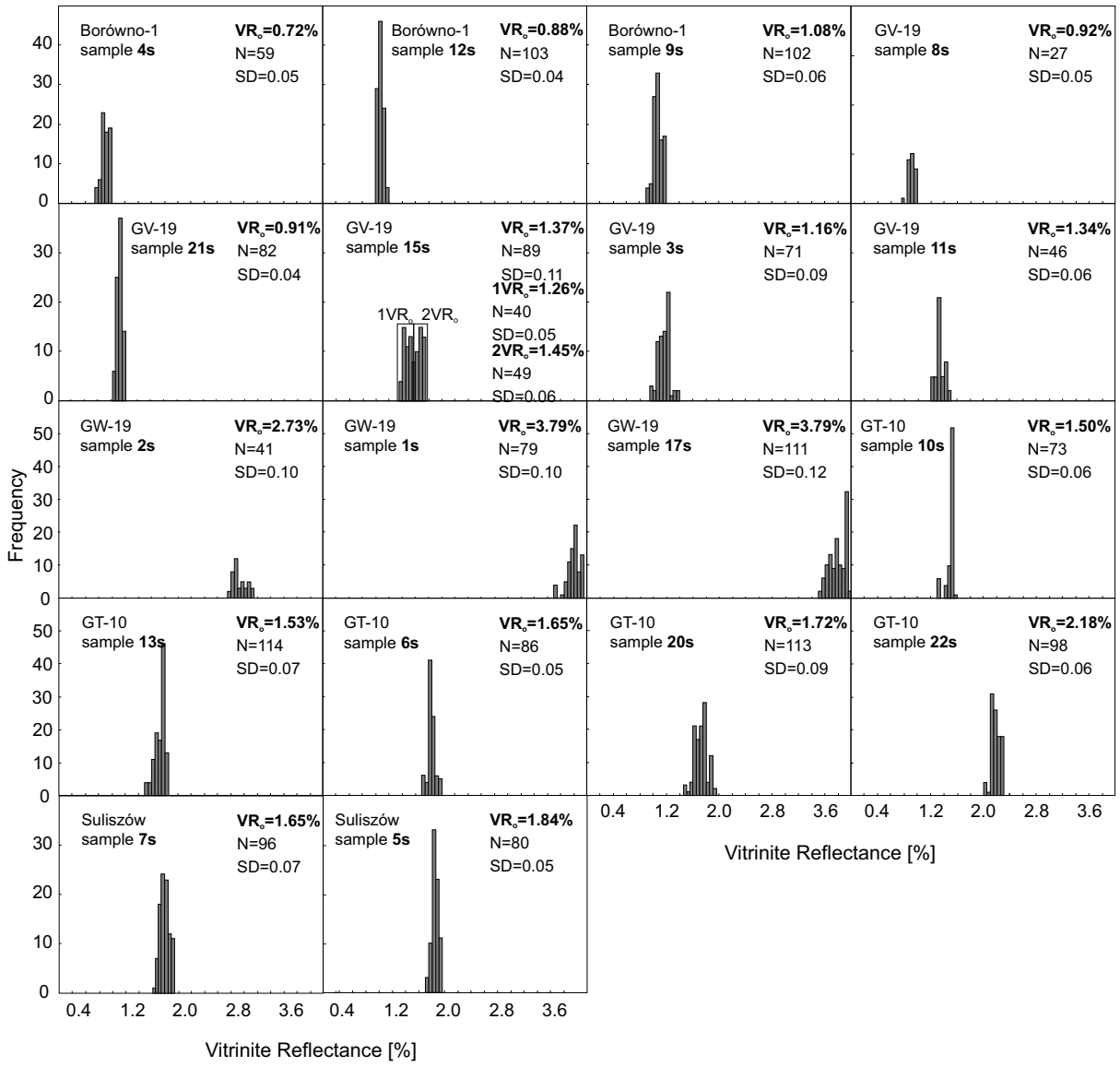

Text-fig. 7. Histograms of mean random vitrinite reflectance measurements. Explanations: VR_o – mean random vitrinite reflectance (%); N – number of measurements, SD – standard deviation; $1VR_o$ – mean random vitrinite reflectance for the first vitrinite population in sample 15s; $2VR_o$ – mean random vitrinite reflectance for the second vitrinite population in sample 15s.

That is the reason why most the satisfactory solution is the polynomial function describing the correlation between VR_o and R'_{max} presented in this study.

The deepest and oldest Carboniferous strata show the highest thermal maturity values (sample 1s and 17s, VR_o = 3.80%), while samples from shallower units gave the lower thermal maturity values (sample 4s has the lowest VR_o = 0.72%; Table 1, Text-fig. 11). The increase of VR_o values with depth is uniform in the analysed wells and the average trend allows us to estimate the VR_o gradient to be c. 0.18% VR_o per 100 m. The VR_o gradient is slightly higher in the best sampled well GT-10 (c. 0.25% VR_o per 100 m; Text-fig. 11).

RAMAN SPECTROSCOPY DATA

Summary of measurements

Raman spectroscopy data of OM from the ISB are presented in Table 5 for 18 measured shale sam-

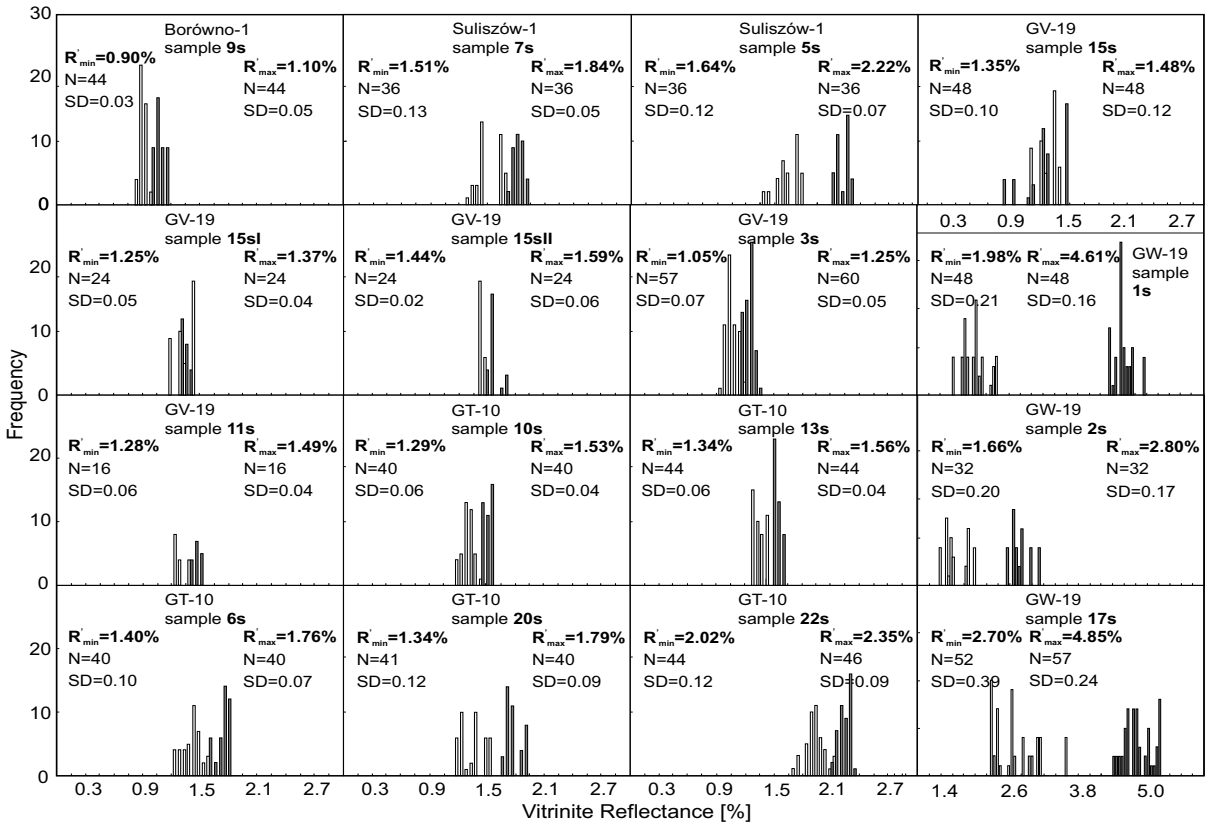

Text-fig. 8. Histograms of R'_{min} and R'_{max} vitrinite reflectance measurements. Explanations: R'_{min} – mean apparent minimum vitrinite reflectance (%); R'_{max} – mean apparent maximum vitrinite reflectance (%); N – number of measurements; SD – standard deviation.

ples. Representative Raman spectra are shown in Text-fig. 12. The Raman data (Table 5 and Text-fig. 12) reflect the continuous ordering of OM by a progressive thermal overprint. With rising temperature, the position of the D1 band shifts to lower values of Raman shift (Text-fig. 12). The position of the G band did not show visible shifts (Text-fig. 12). There is also a distinguishable D4-band in the samples. FWHM-D1 values in the analysed samples are in the range 103.57–146.97 cm^{-1}. The standard deviation of FWHM-D1 ranges from 2.95 to 10.63 with the exception of sample 21s which reaches 14.79. FWHM-G values in the samples are in the range 39.74–60.86 cm^{-1} with standard deviation 0.65–5.49 (Table 5, Text-figs 12, 13). The coefficient of variation (Co.V.), which is also known as relative standard deviation (e.g., Henry *et al.* 2018) of the FWHM-D1 is low and it ranges from 2.22 to 8.43, with the exception of sample 21s which has Co.V. 10.07% (Table 5). The Co.V. of the FWHM-G is also low and it ranges from 1.60 to 9.16% (Table 5). The characteristics of Raman spectra imply that these are highly disordered low-grade OM (e.g., Beyssac *et al.* 2003a, b; Kouketsu *et al.* 2014). Most of the analysed varied organic particles in the given samples show a very uniform Raman spectra pattern, which is supported by their low standard deviation and low Co.V. (Table 5). Generally, uniform distribution FWHM-G and FWHM-D1 are also visible on the histograms (Text-fig. 13). However, in some samples, such as 7s, (borehole Suliszów), 8s (borehole CV-19), and especially 15s, 21s (borehole GV-19) few organic particles show abnormally small D1 and G values of FWHM. This can be attributed to the occurrence of more thermally altered grains, which indicate a higher thermal imprint. These few grains can be redeposited vitrinite or in some cases very small inertodetrinites.

Quality of measurements

The number of measured organic particles, usually vitrinite, in each sample was at least 30 (Table 5). Intra-particle OM variation of the Raman parameters

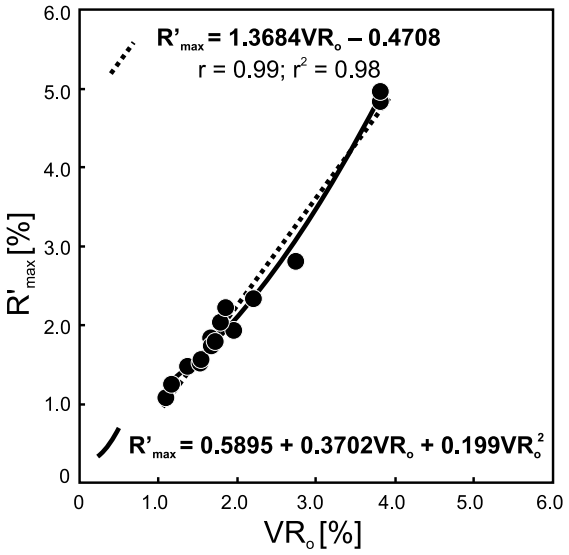

Text-fig. 9. Relationship between random VR_o and maximum R'_{max} vitrinite reflectance. Explanations: Solid line – polynomial regression R'_{max} given VR_o; dashed line – linear regression R'_{max} given VR_o; r – Pearson linear correlation coefficient; r^2 coefficient of determination.

was assessed by the coefficient of variation, which are very low. The Co.V. of the FWHM-D1 band varies from 2.66% (sample 2s) to 10.07% (sample 21s) and the FWHM-G band varies from 1.60% (sample 1s) to 9.16% (sample 21s; Table 5). Low intra-particle OM variation of the Raman parameters emphasizes that almost all measured organic particles belong to one maceral group (vitrinite).

The homogeneity of a single organic particle was measured by Raman spectroscopy on the largest organic grain in the sample 4s (well Borówno-1). The size of the grain (c. 70 × 35 μm) allowed us to carry out measurements in 4 lines with a total of 26 points (Text-fig. 14). The distance between points was about c. 10 μm. The Raman spectra obtained for each point show very low variability. The values of FWHM of the G and D1 bands vary within small ranges i.e. 56.6–57.9 and 131.8–138.3, respectively and hence the calculated temperatures vary in small ranges (Table 6, Text-fig. 14). It should be noted that the variability for D1 (coefficient of variation) is over two times larger than that for the G band. Therefore, with the calculated temperature using the approach of Kouketsu *et al.* (2014), T1 shows more diversity than T2. As in other grains with a degree of coalification below 200°C the temperature T1 is higher than T2. The spatial distribution of temperatures T1 and T2 in each analysed grain shows areas covering several points of higher temperature separated by the areas of lower temperature (Text-fig. 14 inset A and B). The areas for both temperatures differ slightly, but in broad terms, these areas overlap each other within the standard deviation (compare inset A and B on Text-fig. 14).

Temperature estimation

VR_o – based temperature estimation

The mean random vitrinite reflectance values (Table 1) were transformed into maximum palaeotemperatures using the Barker and Pawlewicz (1994) method. Maximum palaeotemperatures were calculated for the regional burial model (T_b, Barker and Pawlewicz 1994) in the range from 109°C (4s sample) to 243°C (17s sample), whilst maximum palaeotemperatures were calculated for the hydrothermal model (T_h, Barker and Pawlewicz 1994) in the range from 110°C (4s sample) to 323°C (17s sample; Table 7). Additionally, maximum palaeotemperatures using the EASY%VR_o (Sweeney and Burnham 1994) method, were also calculated (Table 7). The obtained results of maximum palaeotemperatures are in the range 108–252°C (assuming a heating rate of 10°C/km), and in the range 120–264°C (assuming a heating rate of 1°C/km; Table 7).

Raman spectroscopy-based temperature estimation

In the ISB samples, in the line-shape of the Raman spectra the D2 band is not visible as it appears above 300°C (e.g., Text-fig. 3; Beyssac *et al.* 2002a, 2003a, b; Kouketsu *et al.* 2014). Moreover, the D4 band is very distinctive, and the D1 band is relatively wide, and lower than the G band. The Raman-derived maximum palaeotemperatures (T_{RSOM}), based on the Kouketsu *et al.* (2014) method, vary from 162°C (sample 21s) up to 255°C (17s sample; Table 7) using temperature equation T1 based on FWHM-D1. In contrast using temperature equation T2 (Kouketsu *et al.* 2014) based on FWHM-G, T_{RSOM} vary from 122°C (sample 3s) up to 266°C (17s sample; Table 7). However, above c. 150°C both temperature equations of Kouketsu *et al.* (2014) give generally similar results (Table 7).

Correlation of Raman spectroscopy with vitrinite reflectance data

Both FWMH-D1 and FWMH-G in analysed sample set show relatively good correlation versus depth

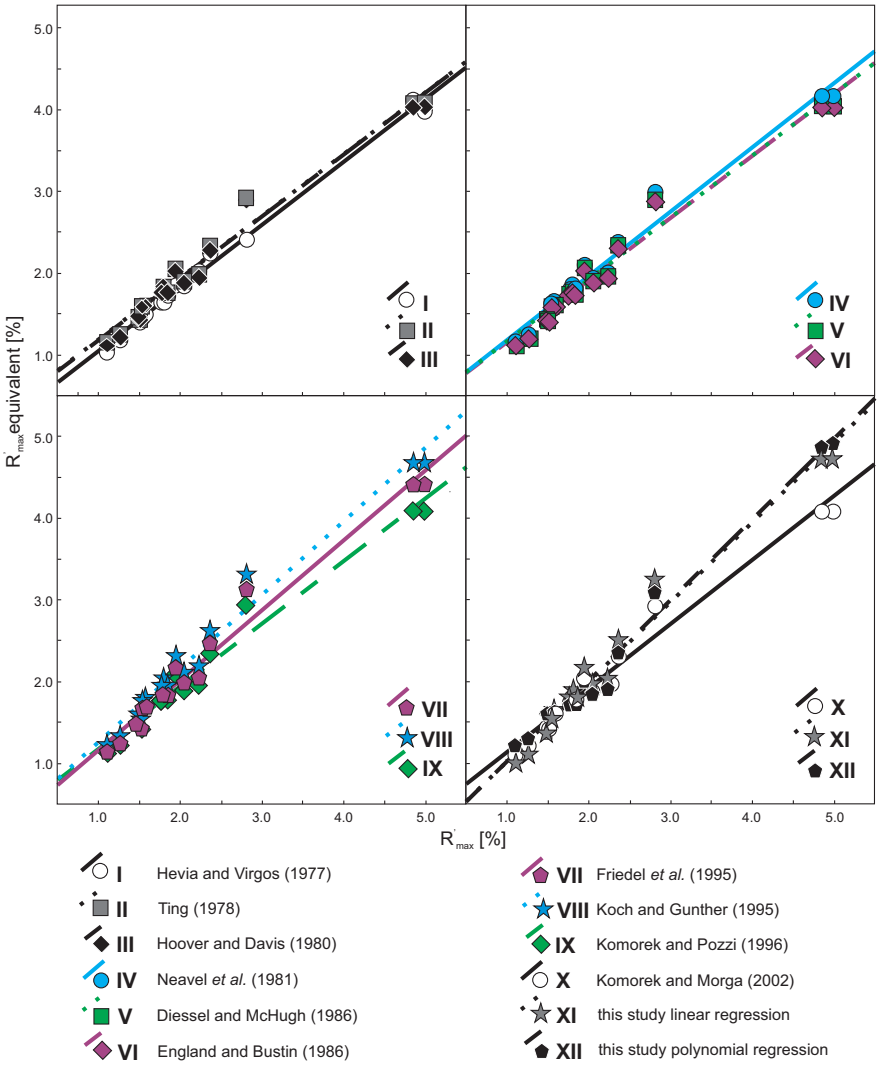

Text-fig. 10. Relationship between measured mean maximum vitrinite reflectance (R'_{max}) and mean maximum vitrinite reflectance (R'_{max} equivalent). Explanations: Converted values applying: I – solid line – Hevia and Virgos (1977) formula $R'_{max} = (3VR_o - R'_{min})/2$; II – small dashed line – Ting (1978) formula $R'_{max} = 1.066*VR_o$; III – large dashed line – Hoover and Davis (1980) formula $R'_{max} = 1.061*VR_o$; IV – solid line – Neavel *et al.* (1981) formula $R'_{max} = 1.06*VR_o - 0.024$; V – small dashed line – Diessel and McHugh (1986) formula $R'_{max} = 1.07*VR_o - 0.01$; VI – large dashed line – England and Bustin (1986) formula $R'_{max} = (VR_o - 0.0011)/0.94$; VII – solid line – Friedel *et al.* (1995) formula $R'_{max} = 1.2*VRo - 1.50$; VIII – small dashed line – Koch and Gunther (1995) formula $R'_{max} = 1.2672*VR_o - 0.1318$; IX – large dashed line – Komorek and Pozzi (1996) formula $R'_{max} = 1.077*VR_o$; X – solid line – Komorek and Morga (2002) formula $R'_{max} = 1.09*VR_o - 0.052$; XI – small dashed line–this study linear regression $R'_{max} = 1.3684*VR_o - 0.4708$; XII – large dashed line – this study polynomial regression $R'max = 0.5895 + 0.3702*VR_o + 0.199*VR_o^2$.

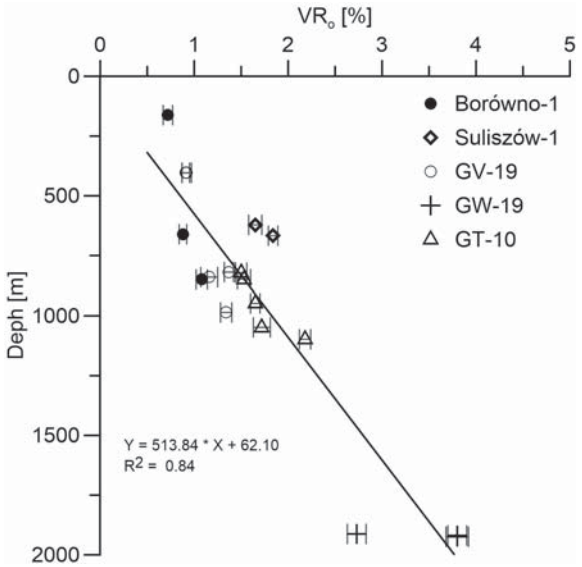

← Text-fig. 11. Mean random vitrinite reflectance versus depth in analysed well sections from the Intra-Sudetic Basin.

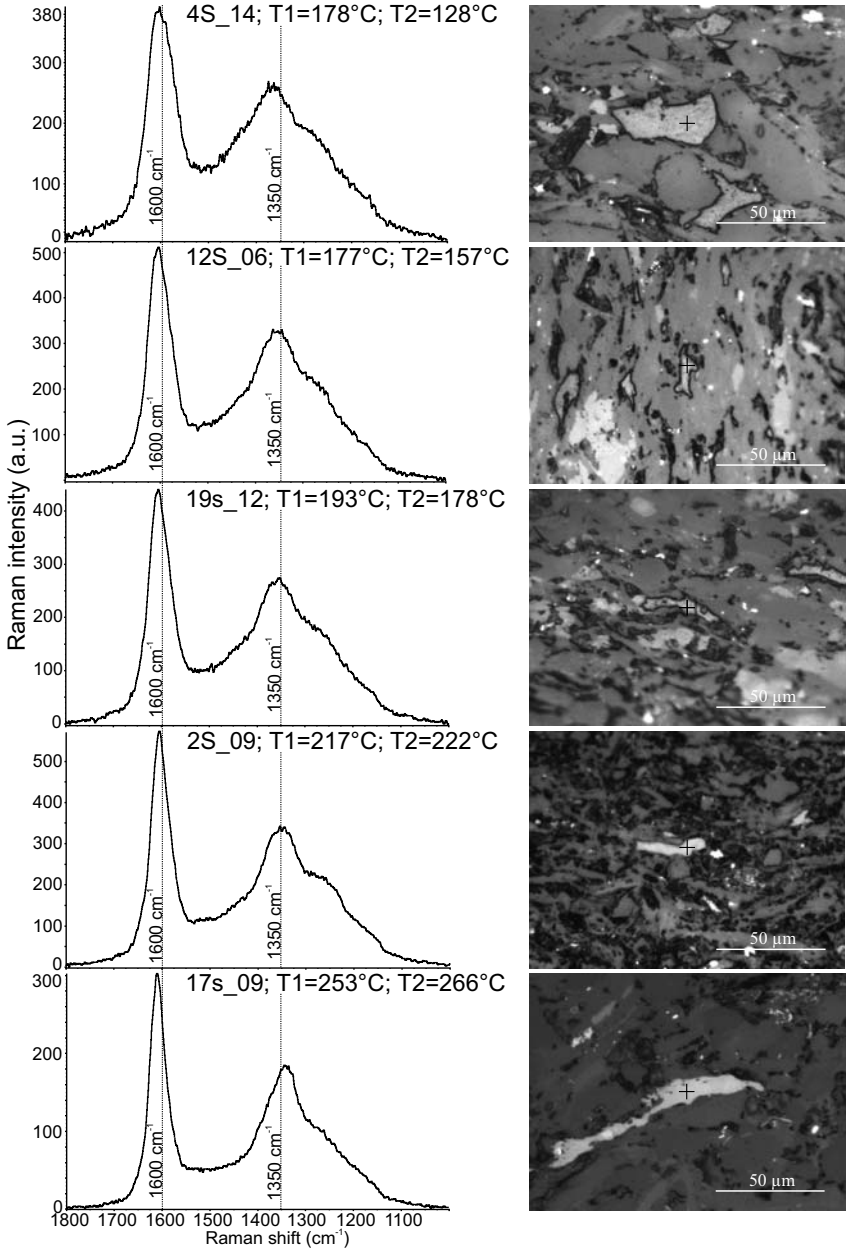

Text-fig. 12. Examples of measured Raman spectra of organic matter and microphotographs showing organic particles in corresponding samples. Note increasing thermal overprint in shale samples.

with r^2 0.72, and 0.78 respectively (Text-fig. 15A, B). Simultaneously also both values FWMH-D1 and FWMH-G show good correlation versus VR_o with $r^2 = 0.84$, and 0.94 respectively (Text-fig. 15C, D). These findings allows to use FWMH-D1 and FWMH-G as a proxy to estimate the thermal maturity of organic matter in a similar manner to the way VR_o is applied. The standard deviation is relatively low and even slightly lower above c. 1.8% VR_o. The change in values of FWMH-D1 up to 2.0%VR_o is small, but it increases in the higher thermal maturity range (c. 2.0–3.8% VR_o). In contrast, the change in FWMH-G seems to be more sensitive both in the diagenetic range below c. 2.0% VR_o and also in the case of more ordered OM, above c. 2.0% VR_o (Text-fig. 15C, D). Because maximum temperatures are calculated using the T1 and T2 equations (Kouketsu *et al.* 2014), which are based on FWMH-D1 and G,

Well	Sample		FWMH (cm^{-1})				Temperature (°C)	
			D4 (1250)	D1 (1350)	D3 (1500)	G (1600)	T1	T2
Borówno-1	4s	Average	165.83	136.97	222.8	60.13	184.0	127.0
		Median	165.38	137.96	216.23	59.62	181.0	131.0
		SD	7.53	9.20	38.37	4.97	19.8	33.7
		Co.V.(%)	4.54	6.72	17.22	8.26	10.8	26.5
	12s	Average	146.03	139.64	221.79	57.49	178.0	145.0
		Median	148.29	139.88	214.21	58.35	177.0	139.0
		SD	9.36	9.51	45.09	4.29	20.5	29.1
		Co.V.(%)	6.41	6.81	20.33	7.47	11.5	20.1
	9s	Average	154.43	143.42	261.56	60.68	170.0	124.0
		Median	153.27	144.44	268.95	61.56	167.0	118.0
		SD	6.16	5.06	21.91	2.32	10.9	15.7
		Co.V.(%)	3.99	3.53	8.38	3.82	6.4	12.7
Suliszów	7s	Average	145.45	136.76	187.94	54.2	184.0	168.0
		Median	141.37	139.53	185.33	55.33	178.0	160.0
		SD	12.63	9.9	18.76	3.23	21.3	21.9
		Co.V.(%)	8.68	7.24	9.98	5.95	11.6	13.1
	5s	Average	145.23	134.38	192.97	53.45	189.0	173.0
		Median	143.64	135.62	193.63	53.47	186.0	172.0
		SD	5.40	7.49	5.23	2.64	16.1	17.9
		Co.V.(%)	3.72	5.57	2.71	4.94	8.5	10.4
GV-19	8s	Average	153.58	144.14	202.17	60.23	168.0	127.0
		Median	153.2	145.56	195.55	59.37	165.0	132.0
		SD	7.90	8.51	29.85	4.18	18.3	28.3
		Co.V.(%)	5.15	5.90	14.77	6.94	10.9	22.4
	21s	Average	151.57	146.97	177.79	59.91	162.0	129.0
		Median	152.60	151.53	174.56	60.09	152.0	128.0
		SD	9.02	14.79	22.11	5.49	31.8	37.2
		Co.V.(%)	5.95	10.07	12.44	9.16	19.6	28.9
	15s	Average	159.73	139.59	205.23	57.07	178.0	148.0
		Median	157.92	139.44	203.58	57.52	178.0	145.0
		SD	14.18	10.10	26.44	2.91	21.7	19.7
		Co.V.(%)	8.88	7.23	12.88	5.09	12.2	13.3
	3s	Average	147.75	145.06	252.45	60.86	166.0	122.0
		Median	148.05	144.56	261.99	60.93	167.0	122.0
		SD	5.16	4.89	33.03	1.43	10.5	9.7
		Co.V.(%)	3.49	3.37	13.08	2.35	6.3	7.9
	11s	Average	176.46	126.14	218,0	56.55	207.0	152.0
		Median	182.3	125.81	228.29	57.18	208.0	147.0
		SD	17.39	10.63	22.63	2.93	22.9	19.9
		Co.V.(%)	9.85	8.43	10.38	5.19	11.1	13.1
GW-19	2s	Average	138.99	122.21	176.93	46.53	215.0	220.0
		Median	137.87	122.52	174.84	46.63	215.0	219.0
		SD	5.59	3.25	5.78	1.31	6.9	8.9
		Co.V.(%)	4.02	2.66	3.27	2.81	3.3	4.1
	1s	Average	167.35	104.4	173.8	40.71	254.0	259.0
		Median	166.73	103.79	175.96	40.6	255.0	260.0
		SD	2.13	2.98	4.53	0.65	6.4	4.4
		Co.V.(%)	1.27	2.86	2.61	1.6	2.5	1.7
	17s	Average	148.74	103.57	179.61	39.74	255.0	266.0
		Median	148.54	103.72	179.43	39.73	255.0	266.0
		SD	2.90	2.95	1.32	0.94	6.3	6.4
		Co.V.(%)	1.95	2.84	0.74	2.38	2.5	2.4

Well	Sample		FWMH (cm^{-1})				Temperature (°C)	
			D4 (1250)	D1 (1350)	D3 (1500)	G (1600)	T1	T2
GT-10	10s	Average	137.29	136.51	184.54	53.3	184.0	174.0
		Median	135.61	140.53	177.09	54.29	176.0	167.0
		SD	7.88	10.30	23.01	3.87	22.2	26.2
		Co.V.(%)	5.74	7.55	12.47	7.26	12.0	15.1
	13s	Average	137.33	134.89	174.34	52.48	188.0	179.0
		Median	136.75	136.6	175.14	53.18	184.0	174.0
		SD	5.21	9.71	5.81	3.21	20.9	21.8
		Co.V.(%)	3.80	7.20	3.33	6.13	11.1	12.2
	6s	Average	141.54	134.26	184.98	52.93	189.0	176.0
		Median	141.14	133.37	185.51	53.46	191.0	173.0
		SD	4.69	7.53	4.29	2.52	16.2	17.1
		Co.V.(%)	3.31	5.61	2.32	4.76	8.6	9.7
	20s	Average	142.25	138.43	192.67	53.82	180.0	170.0
		Median	141.93	139.94	192.61	54.72	177.0	164.0
		SD	2.95	3.90	6.27	1.79	8.4	12.1
		Co.V.(%)	2.07	2.82	3.25	3.33	4.7	7.1
	22s	Average	145.21	135.11	194.53	53.24	188.0	174.0
		Median	144.28	135.16	194.00	53.06	187.0	175.0
		SD	4.24	6.04	5.13	2.13	12.9	14.4
		Co.V.(%)	2.92	4.47	2.64	4.00	6.9	8.3

Table 5. Basic Raman spectroscopy data for samples from the Intra-Sudetic Basin. Explanations: FWHM – full width at half maximum of given band; SD – standard deviation; Co.V. – coefficient of variation. Temperature was calculated based on equations of Kouketsu *et al.* (2014).

	FWMH (cm^{-1})				Temperature (°C)	
	D4 (1250)	D1 (1350)	D3 (1500)	G (1580)	T1	T2
Min. value	155.8	131.8	202.1	56.6	181.0	142.0
Max. value	171.3	138.3	225.1	57.9	195.0	151.0
Average	164.5	135.3	213.9	57.4	187.0	146.0
Median	165.6	135.1	214.2	57.4	188.0	146.0
SD	3.9	1.7	5.5	0.3	3.7	2.1
Co.V. (%)	2.4	1.3	2.6	0.6	1.9	1.5

Table 6. Maximum Raman-derived paleotemperature comparison in one single organic particle from sample 4S (Borówno-1 well). Explanations: FWHM – full width at half maximum of given band; SD – standard deviation; Co.V. – coefficient of variation. Temperature was calculated based on equations of Kouketsu *et al.* (2014).

therefore these Raman-derived temperatures show a similar trend with VR_o (Text-fig. 16). The calculated paleotemperatures VR_o-derived and Raman-derived generally show similar and regular increase trends with depth (Text-fig. 17). Sweeney and Burnham's (1990) approach gave the most uniform results independent of using different heating rate (Text-fig. 17A). The methods of Barker and Pawlewicz (1994) show a significant increased discrepancy between burial-derived temperature and the hydrothermal model (Text-fig. 17B). Kouketsu *et al.*'s (2014) equations seem to give similar results above c. 150°C, but below this value, the T1 equation based on FWMH-D1 overestimates calculated temperature comparing to the T2 equation based on FWMH-G band (Text-fig. 17C).

Paleogeothermal gradient during the Carboniferous–Permian burial

A plot of VR_o against depth (Text-fig. 11) exhibits quite a similar trend in almost all the wells. Additionally, when converting VR_o into temperatures (Table 7) with use of the formulas of Barker and Pawlewicz (1994) the higher values suggest a maximum temperature of c. 109–243°C for the burial

Well	Sample	Depth (m)	VR_o (%)	Temperature (°C)						Average	SD
				Sweeney and Burnham (1990)		Barker and Pawlewicz (1994)		Kouketsu *et al.* (2014)			
				10°C/Ma	1C°/Ma	T_{burial}	T_{hydro}	T1	T2		
Borówno-1	4s	162.2	0.72	108	120	109	110	184	127	126	29
	12s	660.8	0.88	124	140	125	136	178	145	141	20
	9s	850.0	1.08	139	158	142	162	170	124	149	17
Suliszów	7s	621.6	1.65	172	182	176	216	184	168	183	17
	5s	667.0	1.84	182	198	185	230	189	173	193	20
GV-19	8s	403.5	0.92	129	144	129	142	168	127	140	16
	21s	403.9	0.91	129	143	128	140	162	129	138	13
	15s*	819.2	1.37	160	174	161	192	178	148	169	16
	3s	840.1	1.16	145	159	147	171	166	122	152	18
	11s	985.7	1.34	158	172	159	190	207	152	173	21
GW-19	2s	1912.5	2.73	212	228	216	281	215	220	229	26
	1s	1918.8	3.80	252	264	243	323	254	259	266	29
	17s	1924.4	3.80	252	264	243	323	255	266	267	29
GT-10	10s	821.3	1.50	164	178	168	204	184	174	179	14
	13s	848.8	1.53	168	174	170	207	188	179	181	14
	6s	948.0	1.65	172	182	176	216	189	176	185	16
	20s	1048	1.72	176	190	179	222	180	170	186	18
	22s	1098	2.18	195	210	198	252	188	174	203	27

Table 7. Maximum paleotemperatures comparison from VR_o and Raman spectroscopy data. Explanations: VR_o – mean random vitrinite reflectance. Average temperature refers to all calculated values; SD – standard deviation of average temperature.

model (T_b), whilst maximum paleotemperatures were calculated for the hydrothermal model (T_h, Barker and Pawlewicz 1994) in the range 110–323°C, and T_{RSOM}, applying the Kouketsu *et al.* (2014) method, vary from 162 to 255°C based on FWHM-D1. Based on FWHM-G, T_{RSOM} vary from 122 to 266°C (Table 7), assuming that any time dependence is negligible.

By plotting these calculated temperatures against depth (Text-figs 17, 18), temperature gradients for the time of the highest temperatures (paleogeothermal gradient) in the basin can be calculated (Text-fig. 18), assuming that peak thermal maturities were obtained simultaneously in response to sedimentary burial. The inferred paleo-geothermal gradients range from c. 70 to 87°C/km with most clustering around 80°C/km. When considering the influence of time, a higher temperature gradient has to be considered provided that the duration of the highest heat flow is not continuous. These values are much higher than the general global average 30°C/km geothermal gradient for continental crust. The current geothermal gradient, based on temperature measurements in wells located in the ISB, was averaged to be at 25°C/km (Bruszewska 2000). Therefore, a significant change of the temperature gradient during the development of this sedimentary basin is obvious.

DISCUSSION

Raman spectroscopy

Intra-particle OM variation of the Raman parameters have been often discussed in the literature (e.g., Beyssac *et al.* 2003a, b 2004; Aoya *et al.* 2010; Lünsdorf *et al.* 2014). However, our data set shows that the variability of the FWHM-D1 band (Co.V. from 2.66% sample 2s to 10.07% sample 21s) and FWHM-G band (Co.V. from 1.60% sample 1s to 9.16% sample 21s) is low (Table 5). Henry et al. (2018) has also given the relative standard deviation of FWHM, but their values are more scattered in the range c. 4–20%. Our data corresponds very well with the VR_o variation, which also is low (Co.V. from 2.63% in sample 1s to 7.76% in sample 3s, Table 1) and is similar to that observed by others (e.g., Henry *et al.* 2018). It should be noticed, however, that generally mean random vitrinite reflectance measured on dispersed OM in shales usually differs from observed values taken from coal samples of equivalent maturity rank. In particular, VR_o measured on dispersed OM are typically more scattered at higher thermal maturities, particularly above c. 1.50% VR_o (e.g., Scheidt and Littke 1989). The greater dis-

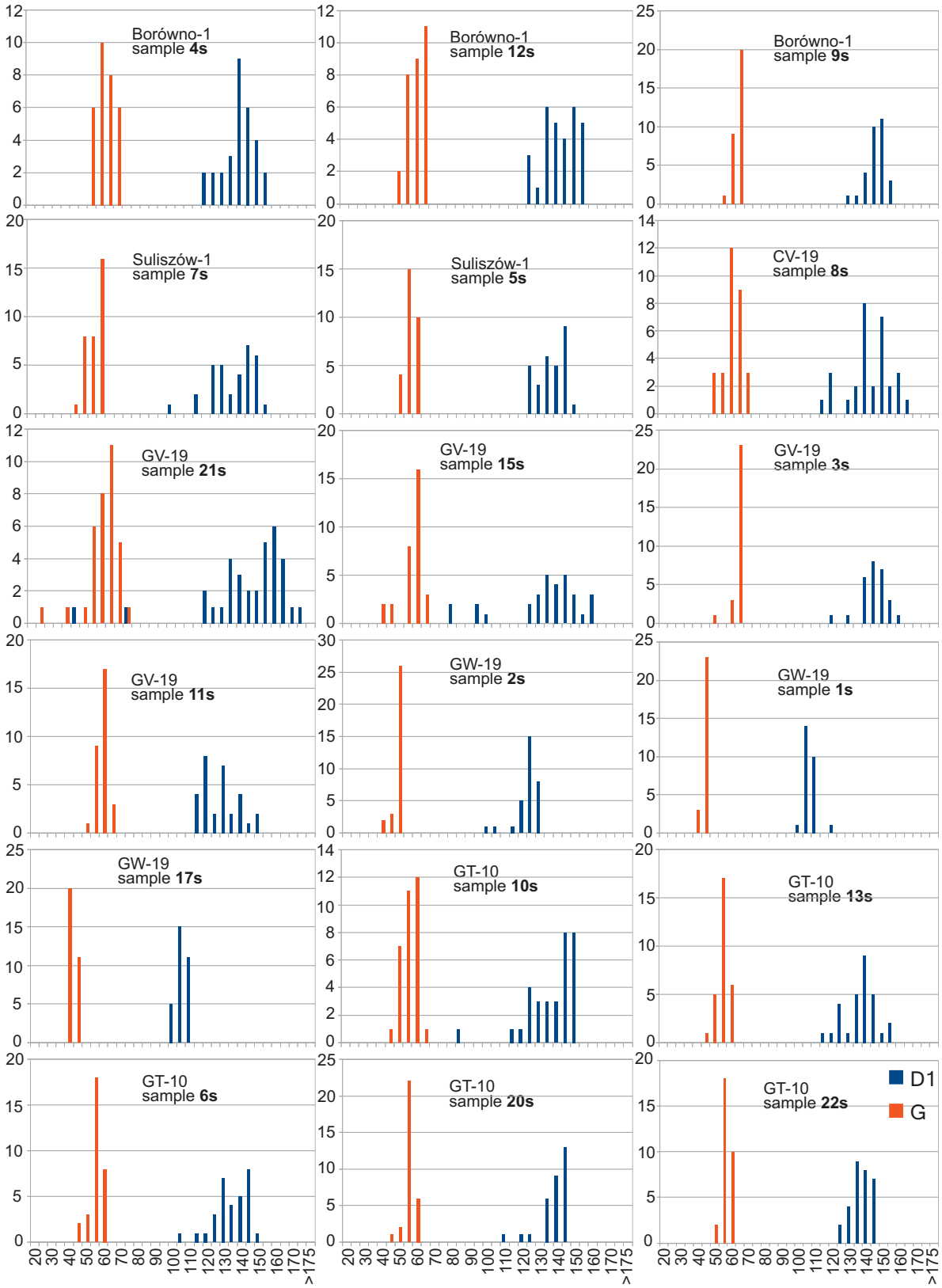

Text-fig. 13. Set of histograms showing full width at half maximum (FWHM) of D1 and G bands in shale samples from the Intra–Sudetic Basin. Each sample histogram is based on measurements of at least 30 organic particles.

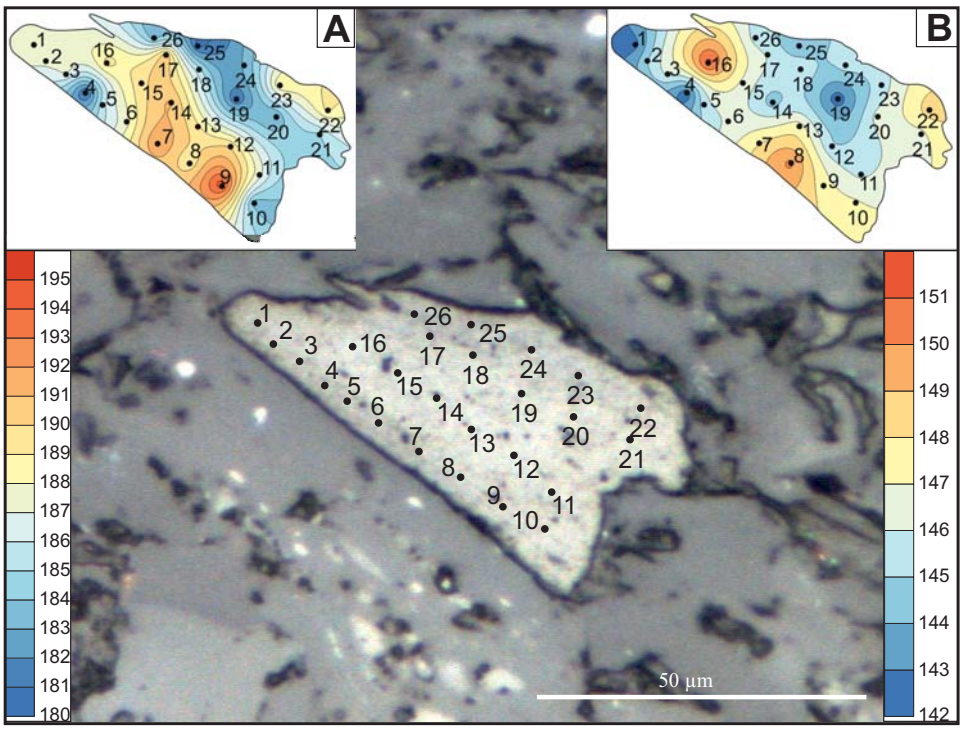

Text-fig. 14. Raman spectroscopy derived paleotemperature for single organic particle in sample 4s from Borówno-1 well. Inset A – map of paleotemperature distribution calculated from FWHM of D1 peak (T1). Inset B – map of paleotemperature distribution calculated from FWHM of G peak (T2).

persion of observed VR_o values at higher thermal maturities (above 1.50% VR_o) can be attributed to several factors, including artefacts due to small particle size or the quality of the polished surface (e.g., Hartkopf-Fröder *et al.* 2015). Applying both Raman spectroscopy and VR_o technique we measured only vitrinite grains. Low variability measured Raman spectroscopy and VR_o data show that analysed samples are relatively homogenous, and vitrinite grains dominate.

Wilkins et al. (2014, 2018) have recently shown the benefits and limitations of applying Raman spectroscopy technique for thermal maturity determination on dispersed OM. One of the most important outcomes of this work is that the discrimination of vitrinite and inertinite is of little importance because thermal maturity values calculated as based on Raman spectroscopy results are obtained by calculations from data combined from both (Wilkins et al. 2014). Therefore, inertinite and vitrinite can be used for thermal maturity determinations by Raman spectroscopy. However, this finding is rather astonishing, because vitrinite reflectance and inertinite reflectance are different, which is a widely well-known phenomena (e.g., Taylor et al. 1998). Therefore, this problem needs further research.

The other important problem considered in some papers (e.g., Beyssac *at al.* 2002b; Aoya *et al.* 2010; Jubb *et al.* 2018) is the heterogeneity of a single organic particle. Beyssac at al. (2002b), based on high-resolution transmission electron microscopy analyses, showed that OM grains show structural heterogeneity but they studied OM grains of high thermal maturity (above 330°C). Using Raman spectroscopy for contact metamorphic rocks and a high transformation temperature, Aoya *et al.* (2010) notice that the R2 ratio can varies considerably in a single grain. In the low temperature transformation Jubb *et al.* (2018) found that the values of FWHM of the D1 band vary considerably in the background minerals, which are stained by organic compounds, but within the OM grain such variation is much smaller. Whereas, the variation of FWHM of the G band is small (Jubb *et al.* 2018). Our test (Text-fig. 14, Table 6) in a single OM grain confirms small variation of temperature distribution in the case of T2 (calculated form FWHM-G) and slightly higher but still low in case of T1 (calculated from FWHM-D1).

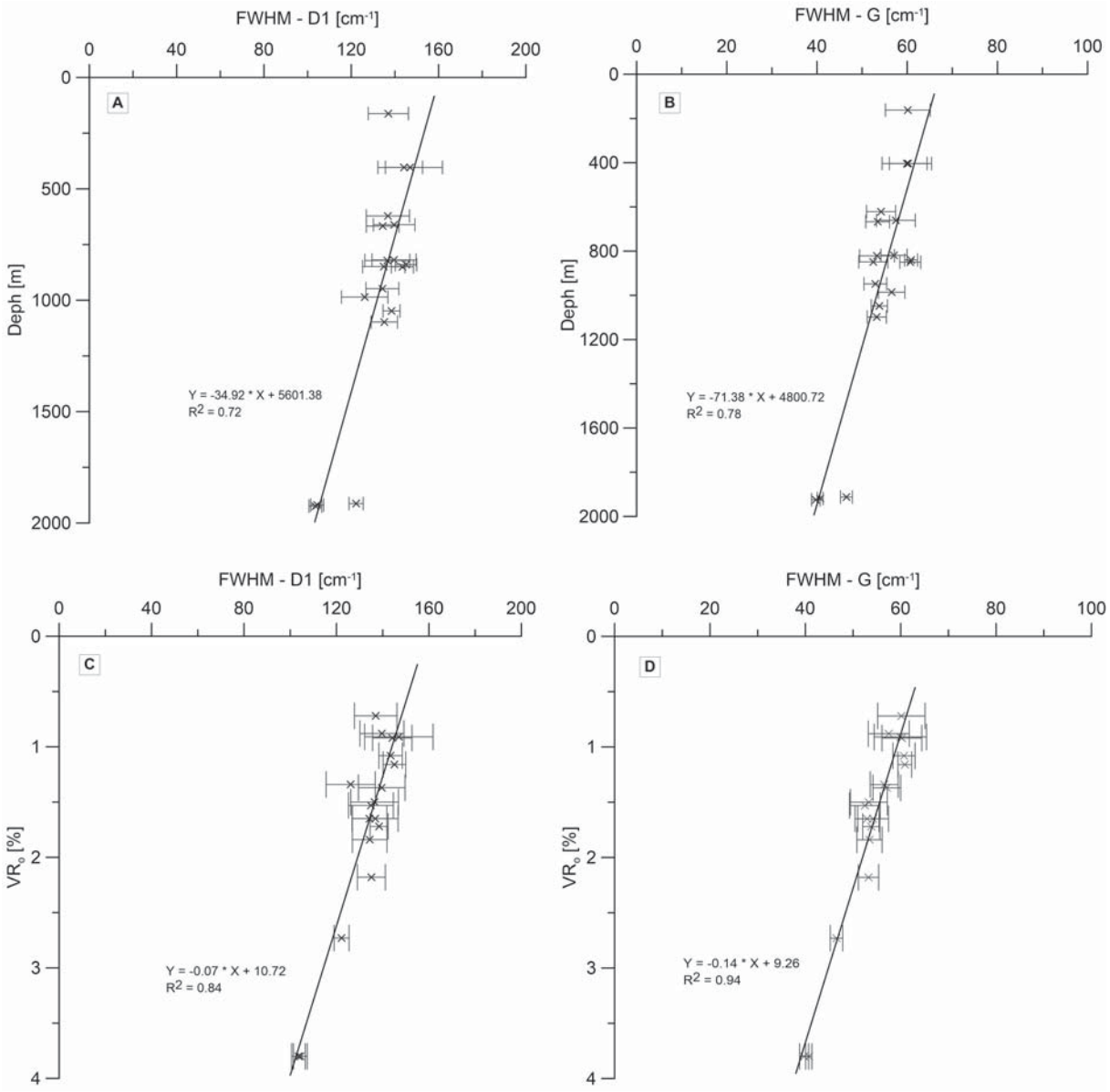

Text-fig. 15. The variability of full width at half maximum (FWHM) of D1 and G bands in the analysed well sections against depth and vitrinite reflectance. A – FWMH-D1 and B – FWMH-G versus depth (including standard deviation); C – FWMH-D1 and D – FWMH-G versus VR_o (including standard deviation).

The performed tests show that analysed organic particles have a high level of homogeneity and a single measurement per one grain is representative.

According to Ferrari and Robertson (2000), the width of the G peak increases as a function of bond-angle disorder at sp^2 sites (in aromatic rings) and its values are the greatest for high sp^3 sites content (aliphatic chains) in highly disordered materials. This parameter increases as a function of decreasing temperature or thermal maturity in regional metamorphism and progressive coalification (Ferrari and Robertson 2000; Beyssac et al. 2002a, b, 2003a, b; Jehlička *et al.* 2003; Guedes *et al.* 2010; Lahfid *et al.* 2010; Wilkins *et al.* 2014; Hinrichs *et al.* 2016; Henry *et al.* 2018, 2019). In agreement with these studies, we observed a decrease of FWHM-G as a function of increasing vitrinite reflectance and burial depth in the diagenetic to late diagenetic zone with

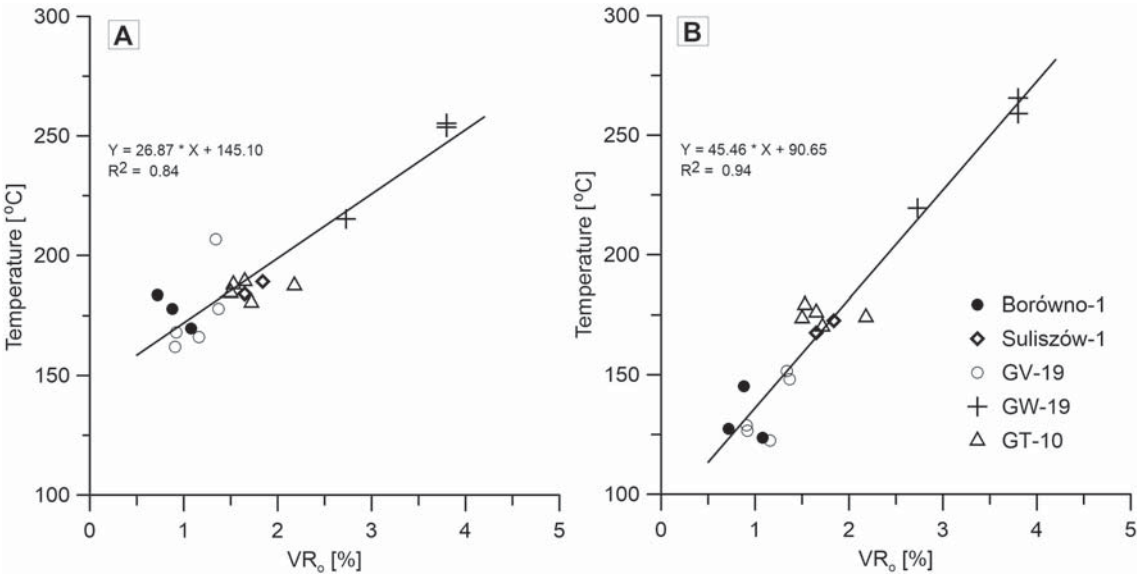

Text-fig. 16. Mean random vitrinite reflectance versus Raman spectroscopy-derived paleotemperature. A – using T1 equation based on FWMH-D1 and B – using T2 equation based on FWMH-G band.

high correlation coefficients (Text-fig. 15). This decrease of FWHM-G is more regular than FWHM-D1. FWHM-G changes systematically from 0.7 to 3.8% VR_o, whereas FWHM-D1 do not show such behaviour until c. 2.0% VR_o.

Vitrinite reflectance

The microscopical study of shale samples from ISB showed that dispersed organic matter in Carboniferous strata is dominated by vitrinite group macerals – a typical feature for coal-bearing environments (e.g., Scheidt and Littke 1989; Taylor *et al.* 1998; Hartkopf-Fröder *et al.* 2015). The vitrinite reflectance is a time-temperature indicator governed by a kinetic response (Sweeney and Burnham 1990). Therefore, vitrinite reflectance continues to increase progressively with increasing temperature, allowing maximum palaeotemperatures to be directly estimated (e.g., Barker and Pawlewicz 1994; Sweeney and Burnham 1990). The mean VR_o values show a uniform increase with depth in analysed wells from ISB (Text-fig. 19). In the lower diagenetic range (below ca. 1% VR_o) both the burial model (T_b, Barker and Pawlewicz 1994) and the hydrothermal model (T_h, Barker and Pawlewicz 1994) have given very similar results. However, the discrepancy between these models is significantly higher in the more advanced diagenesis to early metamorphism phase, particularly above c. 200°C (Table 7, Text-fig. 17). More uniform results were obtained applying the approach of Sweeney and Burnham (1990) as shown in Table 7 and Text-fig. 17.

Vitrinite reflectance anisotropy can be useful for the recognition of the tectonic style of deformation and its relationships to the timing of these processes (e.g., Hower and Davis 1981; Komorek and Pozzi 1996; Komorek and Morga 2002; Komorek and Morga 2007). The measurement of the apparent maximum plus either the apparent minimum or the mean random vitrinite reflectance provides a method for quantification of the anisotropy of the reflectance. This anisotropy may be a direct indicator of static pressure caused by depth of burial, at which coalification occurred. The combination of the thermal record from vitrinite reflectance and pressure information, therefore, provides a means of evaluating the tectonic evolution of a coal seam or sedimentary strata in a basin, given the independent placement of coal-rank parameters on a pressure-temperature framework (Hower and Davis 1981). In the ISB, vitrinite reflectance anisotropy ($VR_b = R'_{max} - R'_{min}$) increases with depth and coal rank (Tables 2–4, Text-figs 7–10). However, in the analysed data set the vitrinite reflectance anisotropy did not change significantly across the region and samples from a similar depth have a similar level of anisotropy (Tables 2–4, Text-figs 7–10), suggesting that it can be correlated

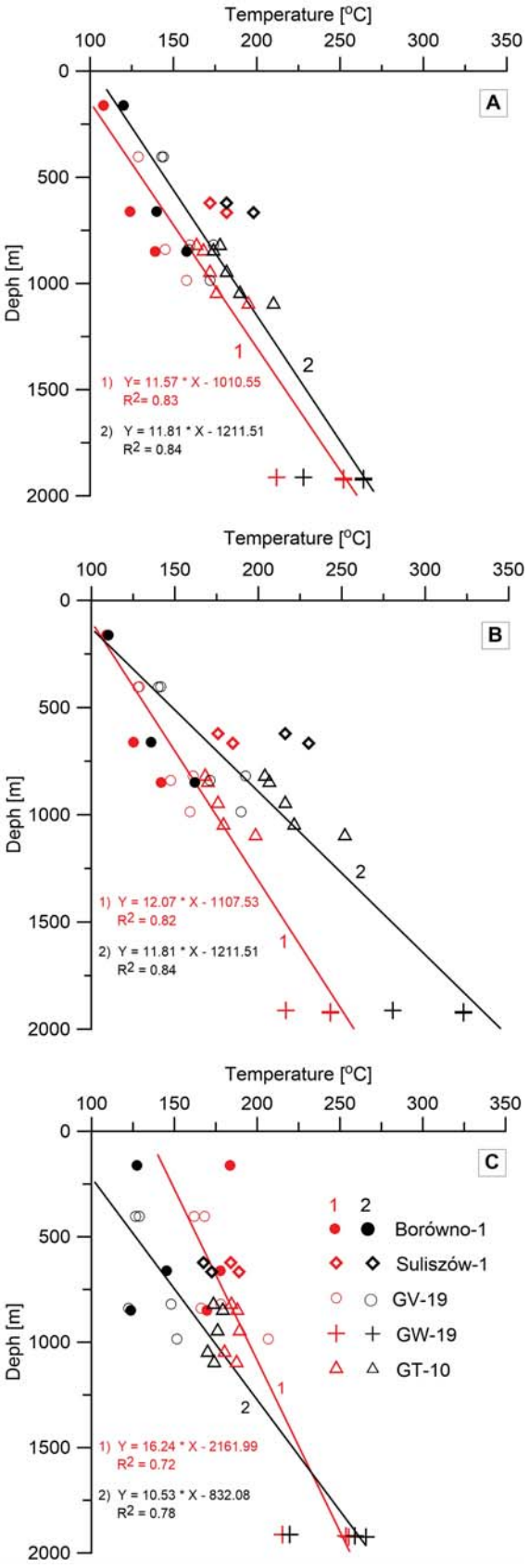

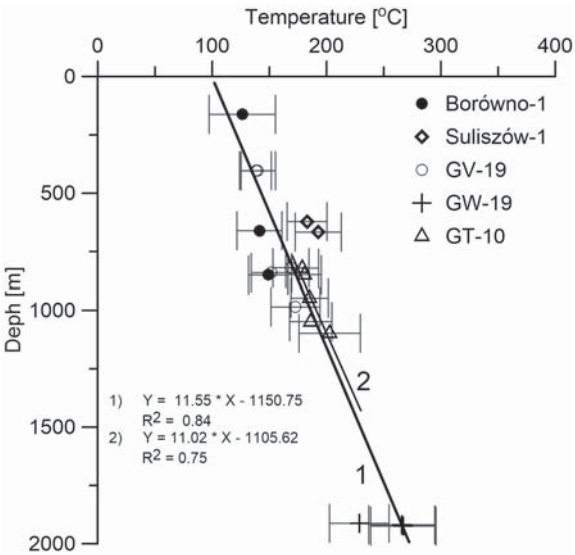

Text-fig. 18. Average paleotemperature versus depth (based on all models from Text-fig. 17) with standard deviation of these six models including average paleotemperature versus depth for GT-10 well.

generally with past depth of burial only and not with directional stress such as in tectonically deformed regions. With increasing of coalification, R'_{max} shows a faster increase of value, whereas R'_{min} increases slowly.

Temperature estimation: Raman spectroscopy versus vitrinite reflectance data

The calculated maximum palaeotemperatures increase with depth in each of the analysed wells (Text-figs 17–18). The T_{RSOM} is compatible with the VR_o–derived palaeotemperature, and depth (Text-figs 11, 16–18). Similar VR_o gradients were calculated also by Mastalerz and Jones (1988) and Nowak (2000) in the ISB. Average VR_o gradients are from c. 0.15 to 0.30% per 100 m, and locally reaching very high values (0.60% per 100 m) in the centre of the basin

← Text-fig. 17. The VRo-derived and Raman-derived paleotemperatures versus depth. Paleotemperatures were calculated applying the following approach. A – Sweeney and Burnham (1990): 1 – regression line was using heating rate of 10°C/km, 2 – regression line was using heating rate of 1°C/km. B – Barker and Pawlewicz (1994): 1 – regression line was calculated using burial model equation: Temperature 1 = ($\ln VR_o$ + 1.68)/0.0124, 2 – regression line was calculated using hydrothermal model equation: Temperature 2 = ($\ln VR_o$ + 1.19)/0.00782. C – Kouketsu *et al.* (2014): 1 – regression line was calculated using T1 equation based on FWMH-D1, 2 – regression line was calculated using T2 equation based on FWMH-G band.

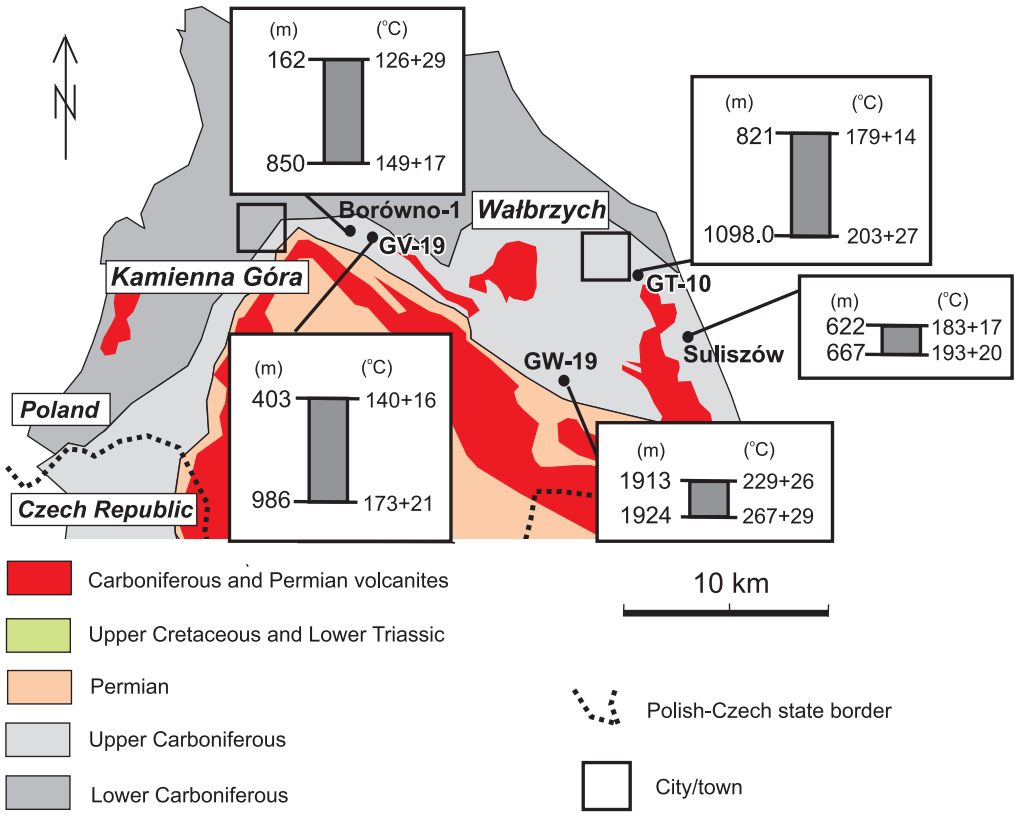

Text-fig. 19. The distribution of maximum paleotemperature of the Carboniferous strata in analysed wells from ISB (based on data from Text-fig. 18).

(Mastalerz and Jones 1988; Nowak 2000). Similar paleogeothermal gradients were calculated based on volatile content in coals (V^{daf}) data by Kułakowski (1979; 90°C/km), and applying VR_o also by Mastalerz and Jones (1988; 80–100°C/km).

The displayed data of the wells (Text-figs 17–18) fit well with a linear gradient and therefore suggest a similar temperature history. Since the overall trend does not show significant anomalies in any direction, it can be concluded that the maximum temperature event occurred after the youngest of the measured samples was deposited. Since the youngest drill core sample on which VR_o was measured is from the latest Carboniferous, this age or a younger maximum temperature event is evident. It should be noted that the estimation of the paleogeothermal gradient in the latest Carboniferous to early Permian was based on a limited number of measurements from individual boreholes. The validity of such an approach is based on the presumption that paleogeothermal gradient was more or less constant over the whole area. However, taking into account the distribution of syn-sedimentary volcanites and the variations in burial depth that once existed across the area, this presumption seems to be a simplification. Taking into account relatively high VR_o gradients in the ISB (Text-fig. 11), such a distribution seems to be related to Variscan burial heating in a high thermal regime setting (Botor 2008), caused by high heat flow due to magmatic activity in late Carboniferous to early Permian times.

Both the Raman-derived maximum palaeotemperature and VR_o data shows increasing thermal maturity of OM from W (Borówno-1 area) to E (Suliszów – GT-10 area), where more significant intrusive bodies occur (Text-fig. 19). Therefore, varied heat flow values could have influenced the thermal maturity of OM. This trend was also noted by Mastalerz and Jones (1988). However, it should be underlined that due to the low number of samples we did not observe any possible influence of direct contact metamorphism, which apparently should operate in the study area. Probably, the analysed samples occurred too far from magmatic bodies.

Thermal overprint related to the temperature of c. 150°C, based on the Kouketsu *et al. (*2014) method, seems to be an important border below which the estimated maximum paleotemperature from Raman spectroscopy data is not very precise and shows significant errors, as was also shown by earlier works (e.g., Kouketsu *et al.* 2014; Lünsdorf *et al.* 2014; Lünsdorf 2016). Therefore, this low diagenetic zone requires further investigations.

Regional context of coalification in the Intra-Sudetic Basin

The paleotemperature record derived from thermal maturity data accomplished by Raman spectroscopy and VR_o, indicates that the Carboniferous sedimentary sequence experienced elevated temperatures in the past that cannot be explained by the present-day low geothermal gradient (c. 25°C/km; Bruszewska 2000) or just by the thickness of the preserved post-Carboniferous overburden. The paleotemperatures have rather to be explained in terms of greater burial depth or a period of elevated heat flow in the past. Late Carboniferous to early Permian intrusions are widely known in the ISB (Awdankiewicz *et al.* 1999a, b 2004; Ulrych *et al.* 2004, 2006, 2011). Additionally, the coal-bearing sequence of the ISB is cut by numerous dykes and sills (e.g., Awdankiewicz *et al.* 1999a, b 2004; Mastalerz and Jones 1988). However, thermally altered coals were observed only in very thin zones adjacent to the intrusive bodies. Therefore, the direct influence of contact metamorphism in relation to the occurrence of these magmatic bodies on the coal rank is very limited (Kwiecińska 1967; Kułakowski 1979; Mastalerz and Jones 1988; Kwiecińska *et al.* 1992; Kwiecińska and Nowak 1997; Nowak 1997, 1998, 2000; Mastalerz and Mastalerz 2000). In the boreholes examined here there is no evidence of the influence of the volcanic rocks on OM thermal maturity within the analysed shales. However, the study did not cover the entire sedimentary successions present in the wells. Moreover, it should be mentioned that sedimentary burial in the studied area was very deep during the Westphalian (Mastalerz and Jones 1988) and could most likely have been responsible for the increase in VR_o independently of the direct effects of the intrusion (Mastalerz and Jones 1988). Present-day values of the geothermal gradient for the ISB vary between 22.6 and 25.4ºC/km and the average value for the Czech part of the ISB is about 24ºC/km (Čermak 1968). Bruszewska (2000) has recently calculated an average geothermal gradient for the ISB of 25ºC/km and a heat flow of 60 mW/m^2. In contrast, high paleogeothermal gradients of c. 80°C/km were calculated based on our data set from dispersed organic matter in shales of the ISB. Similar paleogeothermal gradients (80–100°C/km) were given by coal rank data (Kułakowski 1979; Mastalerz and Jones 1988). Therefore, recent values are over 3 times lower than the calculated values for the late Paleozoic. The reason of such a high paleogeothermal gradient during burial can be related to the high terrestrial heat flow density in the late Paleozoic – which is typical of that of volcanic active areas (Allen and Allen 1990). It seems that although contact metamorphism was very limited, magmatic processes generated this high heat flow regime entirely in the ISB (Dziedzic 1965).

Contemporaneously, the vitrinite reflectance pattern in the shale of the ISB shows that thermal maturity is lower near the margins of basin, and increases towards the centre of this basin. Similar conclusions were given based on the observed trend in isopach maps at the Westphalian B/C transition (Mastalerz and Jones 1988) and on coal rank pattern (Mastalerz and Jones 1988; Nowak 2000). Also VR_o gradients increase towards the centre of ISB i.e. towards the deeper part of the basin (Mastalerz and Jones 1988; Nowak 2000). All these data suggest strongly that one of the most important factors of coalification in the northern part of the ISB (Wałbrzych district) was sedimentary burial during the late Carboniferous. Therefore, on the regional scale of the ISB, two major parameters were critical for coalification: (1) total thickness of Upper Paleozoic sediments and (2) high heat flow due to the tectonic setting related to magmatic bodies. Contact metamorphism contributed only locally to coalification. The heating from the basement is believed to be one of the major reasons for coalification in many basins (e.g., Damberger 1971; Facer *et al.* 1980; Teichmüller 1987; Taylor et al. 1998). Very high Variscan paleogeothermal gradients (c. 100°C/km and above) due to high heat flows have been postulated for a number of domains of the central-western European Variscan orogen (e.g., Dvořák 1989; Robert 1989; Suchý *et al.* 1997). Recent study based on apatite fission track data and coalification data from the northern Czech Republic basins showed that paleogeothermal gradients during the Carboniferous must have indeed been very high, probably around 200°C/km (Suchý *et al.* 2019). During a high heat flow regime, even a relatively low burial depth (c. 800 m; suggested by Mastalerz and Jones 1988) could have caused a significant increase in coalification. Similar conclusions that the

coalification process has started already at a shallow burial depth due to highly elevated Variscan heat flow are given by Pešek and Sýkorová (2006) in the Czech part of Carboniferous and Permian sedimentary basins on the Bohemian Massif. A combination of heat flow and the thickness of post-Westphalian sediments probably allowed coalification to continue during at least the Stephanian or even longer to the early Permian (Botor 2008). Undoubtedly, the ISB was developed during a very hot thermal regime in the Late Paleozoic, as proposed by Dziedzic (1965, 1986).

The heating related to the heat flow that overprinted the organic matter in Carboniferous shale samples was achieved in the late Carboniferous (c. late Westphalian–Stephanian; Kułakowski 1979; Mastalerz and Jones 1988) or latest Carboniferous to early Permian (Botor 2008). This Variscan thermal peak was followed, as indicated by apatite fission track data (Botor *et al.* 2019), by a rather slow cooling in the late Permian–Early Cretaceous with possible long residence in the temperature range c. 60–120°C and final acceleration of cooling in the Late Cretaceous–Paleogene (Botor *et al.* 2019). Similar rapid Late Cretaceous–Paleogene cooling was also shown by thermochronological data in adjacent areas (Danišík *et al.* 2012; Sobczyk *et al.* 2015; 2019; Botor *et al.* 2017b). Therefore, the Variscan heating event, was succeeded by post-Variscan cooling. Consequently, the Cenomanian–Turonian burial most likely did not cause further coalification (Botor *et al.* 2019). The late Carboniferous–early Permian magmatic activity (e.g., Awdankiewicz *et al.* 1999a, b, 2004) responsible for the high heat flow, together with the added effect of significant sedimentary burial in the late Carboniferous–early Permian influenced the coalification processes of Carboniferous organic matter in the ISB. Thermal modelling using apatite fission track data (Danišík *et al.* 2012; Sobczyk *et al.* 2015, 2019; Botor *et al.* 2019) and organic maturity data has shown that the major coalification phase of the Namurian–Westphalian coal seams in the ISB could have occurred in the late Carboniferous to early Permian. The second phase of temperature increase due to Mesozoic sedimentary burial did not exceed the temperatures experienced by the Carboniferous samples in the late Palaeozoic (Danišík *et al.* 2012; Sobczyk *et al.* 2015, 2019; Botor *et al.* 2019). Therefore, the Mesozoic temperature increase does not appear to have any noticeable influence on the maturation of the Carboniferous organic matter in the ISB.

CONCLUSIONS

- The vitrinite maceral group is the main organic component observed in the Carboniferous shales of ISB. The thermal maturity of OM dispersed in the analysed shales is in the range of 0.72 to 3.80% VR_o. However, for most of the analysed samples, the values of the VR_o are characteristic for the OM in the so-called the main generation phase of hydrocarbons. R'_{max} values for the analysed sample set are in the range from 1.10 to 4.98%, whereas the values of the R'_{min} are in the range from 0.90 to 2.70%.
- The most pronounced feature of changes in Raman spectra in the diagenesis to very low-grade metamorphism range consists mainly in a narrowing of the G band region. Moreover, the peak width of the G band (c. 40–61 cm^{-1} with standard deviation of 0.6–5.5) shows very good correlation to mean VR_o. Therefore, FWMH of G band can be widely used as a complementary technique for thermal maturity assessment of organic matter.
- Geological data combined with Raman spectroscopy and vitrinite reflectance results indicate that the Namurian–Westphalian coal-bearing sequence in ISB reached maximum paleotemperatures from c. 110 to c. 265°C. The average regional paleogeothermal gradient in the late Paleozoic was c. 80°C/km.
- The Variscan heating presumably caused major coalification processes of organic matter. The high heat flow, caused by the late Carboniferous–early Permian magmatic activity in the ISB, had an influence on coalification already at the early phase of burial. The heating from the basement seems to be one of the important reasons of coalification, or rather a combination of heat flow from the basement and the thickness of post-Westphalian sediments, which probably allowed coalification to continue during at least the Stephanian or even longer to the early Permian.

Acknowledgements

We thank Dr. Angeles Borrego (Oviedo, Spain), Dr. Jolanta Kus (Hannover, Germany) and Dr. Václav Suchý (Praha, Czech Republic) and Editors of *Acta Geologica Polonica,* particularly Dr. Piotr Łuczyński for their valuable input, which highly improved the quality of the paper. Sincere thanks are due to Mr. J. Szumny, A. Szumny and P. Szumny (AGH, Kraków) for preparation of polished sections of organic matter. This work was partially financed by AGH statutory grants no. 11.11.140.562 and 16.16.140.315.

REFERENCES

Adamczyk, Z., Kokowska-Pawłowska, M., Komorek, J., Klupa, A., Lewandowska, M. and Nowak, J. 2018. The impact of a Neogene basalt intrusion on the optical properties and internal structure of the dispersed organic matter in Carboniferous strata (SW-part USCB). *Acta Geologica Polonica*, **68** (2), 249–262.

American Society For Testing and Materials (ASTM) 2011. Standard test method for microscopical determination of the reflectance of vitrinite dispersed in sedimentary rocks: West Conshohocken, PA. *ASTM International – Annual book of ASTM standards: Petroleum products, lubricants, and fossil fuels; Gaseous fuels; coal and coke*, sec. 5, v. 5.06, No D7708-11, 823–830.

Allen, P.A. and Allen, J.R. 1990. Basin Analysis. Principles & Applications. 451 pp. Blackwell Scientific, Oxford.

Aoya, M., Kouketsu, Y., Endo, S., Shimizu, H., Mizukami, T., Nakamura, D. and Wallis, S. 2010. Extending the applicability of the Raman carbonaceous material geothermometer using data from contact metamorphic rocks. *Journal of Metamorphic Geology*, **28**, 895–914.

Aramowicz, A., Anczkiewicz, A.A. and Mazur, S. 2006. Fission track dating of apatites from the Góry Sowie Massif, Polish Sudetes, NE Bohemian Massif: Implications of post-Variscan denudation and uplift. *Neues Jahrbuch für Mineralogie Abhandlungen*, **182**, 221–229.

Awdankiewicz, M. 1999a. Volcanism in a late Variscan intramontane trough: Carboniferous and Permian volcanic centres of the Intra-Sudetic Basin, SW Poland. *Geologia Sudetica*, **32**, 13–47.

Awdankiewicz, M. 1999b. Volcanism in a late Variscan intramontane trough: the petrology and geochemistry of the Carboniferous and Permian volcanic rocks of the Intra-Sudetic Basin, SW Poland. *Geologia Sudetica*, **32**, 83–111.

Awdankiewicz, M. 2004. Sedimentation, volcanism and subvolcanic intrusions in a late Palaeozoic intramontane trough (the Intra-Sudetic Basin, SW Poland). *Geological Society, London, Special Publications*, **234**, 5–11.

Barker, C. and Pawlewicz, M.J. 1994. Calculation of vitrinite reflectance from thermal histories: a comparison of methods. In: Mukhopadhyay, P.K. and Dow, W.G. (Eds), Vitrinite reflectance as a maturity parameter: applications and limitations, 216–229. American Chemical Society Symposium Series; Washington D.C.

Beny-Bassez, C. and Rouzaud, J.N. 1985. Characterisation of carbonaceous materials by correlated electron and optical microscopy and Raman microspectrometry. *Scanning Electron Microscopy*, **1**, 119–132.

Beyssac, O, Goffe, B., Chopin, C. and Rouzaud, J.N. 2002a. Raman spectra of carbonaceous material in metasediments: a new geothermometer. *Journal of Metamorphic Geology,* **20**, 858–871.

Beyssac, O., Rouzaud, J. N., Goffé, B., Brunet, F. and Chopin, C. 2002b. Graphitization in a high-pressure, low-temperature metamorphic gradient: A Raman microspectroscopy and HRTEM study. *Contributions to Mineralogy and Petrology*, **143**, 19–31.

Beyssac, O., Brunet, F., Petitet, J., Goffé, B. and Rouzaud, J.N. 2003a. Experimental study of the microtextural and structural transformations of carbonaceous materials under pressure and temperature. *European Journal of Mineralogy*, **15**, 937–951.

Beyssac, O., Goffe, B., Petitet, J.P., Froigneux, E., Moreau, M. and Rouzaud, J.N. 2003b. On the characterization of disordered and heterogeneous carbonaceous materials by Raman spectroscopy. *Spectrochimica Acta Part A: Molecular and Biomolecular Spectroscopy*, **59**, 2267–2276.

Birkenmajer, K., Pécskay, Z., Grabowski, J., Lorenc, M.W. and Zagożdżon, P.P. 2004. Radiometric dating of the Tertiary volcanics in Lower Silesia, Poland. IV. Further K-Ar and palaeomagnetic data from Late Oligocene to Early Miocene basaltic rocks of the Fore-Sudetic Block. *Annales Societatis Geologorum Poloniae*, **74**, 1–19.

Bossowski, A. and Ihnatowicz, A. 1994. Palaeogeography of the Upper Carboniferous coal-bearing deposits in NE part of the Intra-Sudetic Depression. *Geological Quarterly*, **38**, 231–248.

Bossowski, A. and Ihnatowicz, A. 2006. Geological Atlas of the Lower Silesian Coal Basin. Państwowy Instytut Geologiczny; Warsaw.

Botor, D. 2008. Thermal history of the coal-bearing Carboniferous rocks in the Wałbrzych district (Lower Silesia Coal Basin, Poland) constrained by numerical maturity modelling – a preliminary results. Conference Proceedings: Górnictwo Zrównoważonego Rozwoju. Gliwice, 20–21.11.2008. *Zeszyty Naukowe Politechniki Śląskiej*, **286**, 15–24. [In Polish with English summary]

Botor, D., Toboła, T. and Jelonek, I. 2017a. Thermal history of the lower Carboniferous Culm Basin in the Nízký Jeseník Mts. (NE Bohemian Massif, Czech Republic and Poland). *Annales Societatis Geologorum Poloniae*, **87**, 13–40.

Botor, D., Dunkl, I., Anczkiewicz, A.A. and Mazur, S. 2017b. Post-Variscan thermal history of the Moravo-Silesian lower Carboniferous Culm Basin (NE Czech Republic – SW Poland). *Tectonophysics*, **712-713**, 643–662.

Botor, D., Anczkiewicz, A.A. Mazur, S. and Siwecki, T. 2019. Post-Variscan thermal history of the Intra-Sudetic Basin (Sudetes, Bohemian Massif) based on apatite fission track analysis. *International Journal of Earth Sciences (formerly Geologische Rundschau*), **108**, 2561–2576.

Bruns, B. and Littke, R. 2015. Lithological dependency and anisotropy of vitrinite reflectance in high rank sedimentary rocks of the Ibbenbüren area, NW-Germany: Implications for the tectonic and thermal evolution of the Lower Saxony Basin. *International Journal of Coal Geology*, **137**, 124–135.

Bruszewska, B. 2000. The geothermal conditions in Lower Silesia (SW Poland). *Przegląd Geologiczny*, **48**, 639–643. [In Polish with English summary]

Carr, A.D. and Williamson P. 1990. The relationship between

aromaticity, vitrinite reflectance and maceral composition of coals: Implications for the use of vitrinite reflectance as a maturation parameter. *Organic Geochemistry*, **16**, 313–323.

Čermak, V. 1968. Heat flow in the Žacler-Svatonovice Basin. *Acta Geophysica Polonica*, **16**, 3–9.

Damberger, H.H. 1971. Coalification pattern of the Illinois Basin. *Economic Geology*, **66**, 488–494.

Danišík, M., Štěpančiková, P. and Evans, N.J. 2012. Constraining long-term denudation and faulting history in intraplate regions by multi-system thermochronology – an example of the Sudetic Marginal Fault (Bohemian Massif, Central Europe). *Tectonics*, **31**, 1–19.

Diessel, C.F.K. and Mchugh, F.A. 1986. Fluoresznezintensitaet und Reflexionsvermoegen von Vitriniten und Inertiniten zur Kennzeichnung des Verkokungsverhaltens. *Glueckauf Forschungshungs*, **47**, 60–70.

Dvořák, J. 1989. Anchimetamorphism in the Variscan tectogene in Central Europe – its relationship to tectogenesis. *Vstník Ústredního Ústavu Geologického*, **64**, 17–30 [in Czech with English abstract]

Dziedzic, K. 1965. Origin of Carboniferous basins on the Gabbro-diabase Nowa Ruda Massif. *Kwartalnik Geologiczny,* **9**, 551–564. [In Polish with English summary]

Dziedzic, K. 1970. Tectonics of the Carboniferous deposits in the north-eastern part of the Nowa Ruda Coal Basin, Sudetes. *Acta Geologica Polonica*, **20** (1), 177–193.

Dziedzic, K. 1971. Sedimentation and paleogeography of the Upper Carboniferous deposits in the Intra-Sudetic depression. *Geologia Sudetica*, **5**, 7–75. [In Polish with English summary]

Dziedzic, K. and Teisseyre, A.K. 1990. The Hercynian mollase and younger deposits in the Intra-Sudetic Basin, SW Poland. *Neues Jahrbuch für Geologie und Paläontologie, Abhandlungen*, **197**, 285–305.

England, T.D.J. and Bustin, R.M. 1986. Thermal maturation of the western Canadian sedimentary basin south Red Deer River – Alberta plains. *Bulletin of Canadian Petroleum Geology*, **34**, 71–90.

Facer, R.A., Cook, A.C. and Beck, A.E. 1980. Thermal properties and coal rank in rocks and coal seams of the southern Sydney Basin, New South Wales: A paleogeothermal explanation of coalification. *International Journal of Coal Geology*, **1**, 1–17.

Ferrari, A.C. and Robertson, J. 2000. Interpretation of Raman spectra of disordered and amorphous carbon. *Physical Review B*, **61**, 95–107.

Franke, W. 1989. Tectonostratigraphic units in the Variscan belt of the Central Europe. *Geological Society American Special Papers*, **230**, 67–90.

Friedel, C.H., Hoth, P., Franz, G. and Stedingk, K. 1995. Niedriggradige Regionalmetamorphose im Harz. *Zentrallblat für Geologische und Paläontologische. Part 1*, **9/10**, 1213–1235.

Grocholski, A. and Augustyniak, K. 1971. Geological Atlas of the Lower Silesian Coal Basin. Wydawnictwa Geologiczne. Warszawa. [In Polish with English summary]

Guedes, A., Valentim, B., Prieto, A.C., Rodrigues, S. and Noronha, F. 2010. Micro-Raman spectroscopy of collotelinite, fusinite and macrinite. *International Journal of Coal Geology*, **83**, 415–422.

Hackley, P.C., Araujo, C.V., Borrego, A.G., Bouzinos, A., Cardott, B.J., Cook, A.C., Eble, C., Flores, D., Gentzis, T., Gonçalves, P.A., Mendonça Filho, J.G., Hámor-Vidó, M., Jelonek, I., Kommeren, K., Knowles, W., Kus, J., Mastalerz, M., Menezes T.R., Newman, J., Oikonomopoulos, J.K., Pawlewicz, M., Pickel, W., Potter, J., Ranasinghe, P., Read, H., Reyes, J., De La Rosa Rodriguez, G., de Souza, I.V.A.F., Suárez-Ruiz, I., Sýkorová I. and Valentine, B.J. 2015. Standardization of reflectance measurements in dispersed organic matter: Results of an exercise to improve interlaboratory agreement. *Marine and Petroleum Geology*, **59**, 22–34.

Hartkopf-Fröder, C., Königshof, P., Littke, R. and Schwarzbauer, J. 2015. Optical thermal maturity parameters and organic geochemical alteration at low-grade diagenesis to anchimetamorphism: A review. *International Journal of Coal Geology,* **150-151**, 74–119.

Henry, D.G., Jarvis, I., Gillmore, G., Stephenson, M., Emmings, J. 2018. Assessing low maturity organic matter in shales using Raman spectroscopy: Effects of sample preparation and operating procedure. *International Journal of Coal Geology*, **191,** 135–151.

Henry, D.G., Jarvis, I., Gillmore, G. and Stephenson, M. 2019. A rapid method for determining organic matter maturity using Raman spectroscopy: Application to Carboniferous organic-rich mudstones and Coals. *International Journal of Coal Geology*, **203**, 87–98.

Hevia, V. and Virgos, J.M. 1977. The rank and anisotropy of anthracites: the indicating surface of reflectivity in uniaxial and biaxial substances. *Journal of Microscroscopy*, **109**, 23–28.

Hinrichs, R., Brown, M.T., Vasconcellos, M.A.Z., Abrashev, M.V. and Kalkreuth, W. 2014. Simple procedure for an estimation of the coal rank using micro-Raman spectroscopy. *International Journal of Coal Geology*, **136**, 52–58.

Houseknecht, D.W., Bensley, D.F., Hathon, L.A. and Kastens, P.H. 1993. Rotational reflectance properties of Arkoma Basin dispersed vitrinite: insights for understanding reflectance populations in high thermal maturity regions. *Organic Geochemistry*, **20**, 187–196.

Hoover, D.S. and Davis, A. 1980. The development and evaluation of an automated reflectance microscope system for the petrographic characterization of bituminous coals. *Penn State University and U.S. Department of Energy Technical Report*, FE-20-30-TR23, 261.

Hower, J.C. and Davis, A. 1981. Application of vitrinite reflectance anisotropy in the evaluation of coal metamorphism. *Bulletin of Geological Society of America*, **92**, 350–366.

International Committee For Coal And Organic Petrology (ICCP). 1998. The new vitrinite classification (ICCP System 1994). *Fuel*, **77**, 349–358.

International Committee for Coal and Organic Petrology (ICCP). 2001. The new inertinite classification (ICCP System 1994). *Fuel*, **80**, 459–471.

Jarmołowicz-Szulc, K, Hałas, S. and Wojtowicz, A. 2009. Radiometric age analyses of rocks from the northern envelope of the Karkonosze Massif, the Sudetes, Poland: a comparative geochronological study. *Geochronometria*, **34**, 33–39.

Jarmołowicz-Szulc, K. 1984. Geochronological study of the northern cover of the Karkonosze granite by fission track method. *Archiwum Mineralogiczne*, **39**, 139–183.

Jehlička, J., Urban, O. and Pokorný, J. 2003. Raman spectroscopy of carbon and solid bitumens in sedimentary and metamorphic rocks. *Spectrochimica Acta Part A*, **59**, 2341–2352.

Jubb, A.M., Botterell, P.J., Birdwell, J.E., Burruss, R.C., Hackley, P.C., Valentine, B.J., Hatcherian, J.J. and Wilson S.A. 2018. High microscale variability in Raman thermal maturity estimates from shale organic matter. *International Journal of Coal Geology*, **199**, 1–9.

Katagiri, G., Ishida, H. and Ishitani A. 1988. Raman spectra of graphite edge planes. *Carbon*, **26**, 565–71.

Kley, J. and Voigt T. 2008. Late Cretaceous intraplate thrusting in central Europe: effect of Africa-Iberia-Europe convergence, not Alpine collision. *Geology*, **36**, 839–842.

Koch, J. and Günther, M. 1995. Relationship between random and maximum vitrinite reflectance. *Fuel*, **74**, 1687–1691.

Komorek, J. and Pozzi, M. 1996. Optical anisotropy of coal from the Jastrzębie Fold (Upper Silesian Coal Basin). *Geological Quarterly*, **40**, 393–406.

Komorek, J. and Morga, R. 2002. Relationship between the maximum and the random reflectance of vitrinite for coal from the Upper Silesian Coal Basin (Poland). *Fuel*, **81**, 969–971.

Komorek, J. and Morga, R. 2007. Evolution of optical properties of vitrinite, sporinite and semifusinite in response to heating under inert conditions. *International Journal of Coal Geology*, **71**, 389–404.

Kouketsu, Y., Mizukami, T., Mori, H., Endo, S., Aoya, M., Hara, H., Nakamura, D. and Wallis, S. 2014. A new approach to develop the Raman carbonaceous material geothermometer for low-grade metamorphism using peak width. *Island Arc*, **23**, 33–50.

Kułakowski, T. 1979. Geological environments of coalification of the Žacléř Beds in the Lower Silesian Coal Basin. *Geologia Sudetica*, **14**, 103–139. [In Polish with English summary]

Kwiecińska, B. 1967. Coked coals from the Wałbrzych Basin. *Prace Mineralogiczne*, **9**, 1–81. [In Polish with English summary]

Kwiecińska, B. Hamburg, G. and Vleeskens, J.M. 1992. Formation temperatures of natural coke in the Lower Silesian Coal Basin, Poland: Evidence from pyrite and clays by SEM-EDX. *International Journal of Coal Geology*, **21**, 217–235.

Kwiecińska, B. and Nowak, G. 1997. Highly metamorphosed coals from the Lower Silesian Coal Basin (SW Poland). *Prace Państwowego Instytutu Geologicznego*, **157**, 247–255.

Lahfid, A., Beyssac, O., Deville, E., Negro, F., Chopin, C. and Goffé, B. 2010. Evolution of the Raman spectrum of carbonaceous material in low-grade metasediments of the Glarus Alps (Switzerland). *Terra Nova*, **22**, 354–360.

Littke, R., Urai, J.L., Uffmann, A.K. and Risvanis, F. 2012. Reflectance of dispersed vitrinite in Palaeozoic rocks with and without cleavage: Implications for burial and thermal history modelling in the Devonian of Rursee area, northern Rhenish Massif, Germany. *International Journal of Coal Geology*, **89**, 41–50.

Lorenz, S. and Mroczkowski, J. 1978. The sedimentation and petrography of Zechstein and lowermost Triassic deposits in the vicinity of Kochanów (Intra-Sudetic Trough). *Geologia Sudetica*, **13**, 23–39.

Lünsdorf, N.K. and Lünsdorf, J.O. 2016. Evaluating Raman spectra of carbonaceous matter by automated, iterative curve-fitting. *International Journal of Coal Geology*, **160-161**, 51–62.

Lünsdorf, N.K. 2016. Raman spectroscopy of dispersed vitrinite – Methodical aspects and correlation with reflectance. *International Journal of Coal Geology*, **153**, 75–86.

Lünsdorf, N. K., Dunkl, I., Schmidt, B. C., Rantitsch, G. and von Eynatten, H., 2014. Towards a higher comparability of geothermometric data obtained by Raman spectroscopy of carbonaceous material. Part I: evaluation of biasing factors. *Geostandards and Geoanalitycal Research*, **38**, 73–94.

Lupoi, J.S., Fritz, L.P., Parris, T.M., Hackley, P.C., Solotky, L., Eble, C.F. and Schlaegle, S. 2017. Assessment of thermal maturity trends in Devonian–Mississippian source rocks using Raman spectroscopy: limitations of peak-fitting method. *Frontiers in Energy Research*, **5**, 1–24.

Malkovský, M. 1987. The Mesozoic and Tertiary basins of the Bohemian Massif and their evolution. *Tectonophysics*, **137**, 31–42.

Maluski, H., Rajlich, P. and Souček, J. 1995. Pre-Variscan, Variscan and early Alpine thermo-tectonic history of the north-eastern Bohemian massif: an Ar/Ar study. *Geologische Rundschau*, **84**, 345–358.

Mastalerz, M. and Jones, J.M. 1988. Coal rank variation in the Intra-Sudetic Basin, SW Poland. *International Journal of Coal Geology*, **10**, 79–97.

Mastalerz, M. and Smyth, M. 1988. Petrography and depositional conditions of the 64/65 coal seam in the Intra-Sudetic Basin, SW Poland. *International Journal of Coal Geology*, **10**, 309–336.

Mastalerz, M. and Wilks, K.R. 1992. Coal seams of the Wałbrzych Formation, Intra-sudetic Basin, Poland: inferences on changing depositional environment. *International Journal of Coal Geology*, **20**, 243–261.

Mastalerz, K. and Mastalerz, M. 2000. Volcanic and post-volcanic hydrothermal activity in the Intra-Sudetic basin, SW Poland: implications for mineralization. In: Glikson, M.V.

and Mastalerz, M. (eds.), Organic Matter and Mineralisation, 185–202, Kluwer Press; Brussels.

Matthews, M.J., Pimenta, M.A., Dresselhaus, G., Dresselhaus, M.S. and Endo, M. 1999. Origin of dispersive effects of the Raman D band in carbon materials. *Physical Review B*, **59**, 6585–6588.

Mazur, S, Aleksandrowski, P., Turniak, K. and Awdankiewicz, M. 2007. Geology, tectonic evolution and Late Palaeozoic magmatism of Sudetes – an overview. In: Kozłowski, A. and Wiszniewska, J. (eds), Granitoids in Poland, 59–87, AM Monography; Warsaw.

Mazur, S, Aleksandrowski, P, Kryza, R. and Oberc-Dziedzic, T. 2006. The Variscan Orogen in Poland. *Geological Quarterly*, **50**, 89–118.

Migoń, P. and Danišík, M. 2012. Erosional history of the Karkonosze Granite Massif – constraints from adjacent sedimentary basins and thermochronology. *Geological Quarterly*, **56**, 440–454.

Migoń, P. and Lidmar-Bergström, K. 2001. Weathering mantles and their significance for geomorphological evolution of central and northern Europe since the Mesozoic. *Earth Sciences Reviews*, **56**, 285–324.

Morga, R. 2011. Micro-Raman spectroscopy of carbonized semifusinite and fusinite. *International Journal of Coal Geology*, **87**, 253–267.

Morga, R. 2014. Raman microspectroscopy of funginite from the Upper Silesian Coal Basin (Poland). *International Journal of Coal Geology*, **131**, 65–70.

Morga, R., Jelonek, I., Kruszewska, K. and Szulik, W. 2015. Relationship between quality of coals, resulting cokes, and micro-Raman spectral characteristics of these cokes. *International Journal of Coal Geology*, **144**, 130–137.

Neaval, R. C. Smith, S. Hippo, E. and Miller, R. 1981. Optimum classification of coal. International Conference of Coal Sciences; Dusseldorf.

Nemanich, R.J. and Solin, S.A. 1979. First- and second-order Raman scattering from finite-size crystals of graphite. *Physical Review B*, **20**, 392–401.

Nowak, G.J. 1993. Lithotype variation and petrography of coal seams from Žacleř Formation (Westphalian) in the Intra-Sudetic Basin, southwestern Poland. *Organic Geochemistry* **20**, 295–313.

Nowak, G.J. 1996. Petrological coal seam accumulation model for the Žacleř Formation of the Lower Silesian Coal Basin, southwestern Poland. In: Gayer, R. and Harris, I. (eds), *Geological Society, London, Special Publications,* **109**, 261–286.

Nowak, G.J. 1997a. Petrology of Žacleř formation coal seams in the Intra-Sudetic Basin (Lower Silesian Coal Basin). *Acta Universitatis Wratislaviensis No 1938. Prace Geologiczno-Mineralogiczne*, **57**, 99 pp. [In Polish with English summary]

Nowak, G.J. 1997b. The variation in coal rank and petrographic composition of coal seams from the eastern part of the Lower Silesian Coal Basin. *Biuletyn Państwowego Instytutu Geologicznego*, **375**, 61–79. [In Polish with English summary]

Nowak, G.J. 2000. Thermal maturity of coals from the Lower Silesian Coal Basin on the background of their petrography and genesis. *Biuletyn Państwowego Instytutu Geologicznego*, **391**, 89–146. [In Polish with English summary]

Opluštil, S. and Cleal, C.J. 2007. A comparative analysis of some Late Carboniferous basins of Variscan Europe. *Geological Magazine*, **144**, 417–448.

Opluštil, S., Schmitz, M., Kachlík, V., and Štamberg, S. 2016. Re-assessment of lithostratigraphy, biostratigraphy, and volcanic activity of the Late Paleozoic Intra-Sudetic, Krkonoše-Piedmont and Mnichovo Hradiště basins (Czech Republic) based on new U-Pb CA-ID-TIMS ages. *Bulletin of Geosciences*, **91**, 399–432.

Pasteris, J. D. and Wopenka, B. 1991. Raman spectra of graphite as indicates of degree of metamorphism. *Canadian Mineralogist*, **29**, 1–9.

Pešek, J. and Sivek, M. 2016. Coal-bearing basins and coal deposits of the Czech Republic. 208 pp. Czech Geological Survey, Prague.

Pešek, J. and Sýkorová, I. 2006. A review of the timing of coalification in the light of coal seam erosion, clastic dykes and coal clasts. *International Journal of Coal Geology*, **66**, 13–34.

Pickel, W., Kus, J., Flores, D., Kalaitzidis, S., Christanis, K., Cardott, B. J., Misz-Kennan, M., Rodrigues, S., Hentschel, A., Hamor-Vido, M., Crosdale, P. and Wagner, N. 2017. Classification of liptinite – ICCP System 1994. *International Journal of Coal Geology*, **169**, 40–61.

Pimenta, M. A., Dresselhaus, G., Dresselhaus, M. S., Cancado, L. G., Jorio, A. and Saito, R. 2007. Studying disorder in graphite-based systems by Raman spectroscopy. *Physical Chemistry and Chemical Physics*, **9**, 1276–1291.

Pócsik, I., Hundhausen, M., Koos, M. and Ley, L. 1998. Origin of the D peak in the Raman spectrum of microcrystalline graphite. *Journal of Non-Crystalline Solids*, **227-230**, 1083–1086.

Potgieter-Vermaak, S., Maledi, N., Wagner, N., Van Heerden, J. H. P., Van Grieken, R. and Potgieter, J.H. 2011. Raman spectroscopy for the analysis of coal: a review. *Journal of Raman Spectroscopy*, **42**, 123–129.

Pusz, S., Borrego, A. G., Alvarez, D., Camean, I., du Cann, V., Duber, S., Kalkreuth, W., Komorek, J., Kus, J., Kwiecińska, B. K., Libera, M., Marques, M., Misz-Kennan, M., Morga, R., Rodrigues, S., Smędowski, Ł., Suarez-Ruiz, I. and Strzezik, J. 2014. Application of reflectance parameters in the estimation of the structural order of coals and carbonaceous materials. Precision and bias of measurements derived from the ICCP structural working group. *International Journal of Coal Geology*, **131**, 147–161.

Rahl, J. M., Anderson, K. M., Brandon, M. T. and Fassoulas, C. 2005. Raman spectroscopic carbonaceous material thermometry of low-grade metamorphic rocks: Calibration and application to tectonic exhumation in Crete, Greece. *Earth and Planetary Science Letters*, **240**, 339–354.

Reich, S. and Thomsen, Ch. 2004. Raman spectroscopy of graphite. *Philosophical Transactions of the Royal Society, London*, **362**, 2271–2288.

Robert, P. 1989. The thermal setting of Carboniferous basins in relation to the Variscan orogeny in Central and Western Europe. *International Journal of Coal Geology*, **13**, 171–206.

Sadezky, A., Muckenhuber, H., Grothe, H., Niessner, R. and Pöschl, U. 2005. Raman microspectrometry of soot and related carbonaceous materials: spectral analysis and structural information. *Carbon,* **43**, 1731–1742.

Sawicki, L. 1995. Geological map of Lower Silesia with adjacent Czech and German territories (without Quaternary deposits) 1:100 000. Państwowy Instytut Geologiczny, Warszawa.

Scheidt, G. and Littke, R. 1989. Comparative organic petrology of interlayered sandstones, siltstones, mudstones and coals in the Upper Carboniferous Ruhr basin, Northwest Germany, and their thermal history and methane generation. *Geologische Rundschau*, **78**, 375–390.

Scheck, M., Bayer, U., Otto, V., Lamarche, J., Banka, D. and Pharaoh, T. 2002. The Elbe Fault System in North Central Europe – a basement controlled zone of crustal weakness. *Tectonophysics*, **360**, 281–299.

Skoček, V. and Valečka, J. 1983. Palaeogeography of the Late Cretaceous Quadersandstein of central Europe. *Palaeogeography, Palaeoclimatology, Palaeoecology*, **44**, 71–92.

Sobczyk, A., Danišík, M., Aleksandrowski, P. and Anczkiewicz, A. 2015. Post-Variscan cooling history of the central Western Sudetes (NE Bohemian Massif, Poland) constrained by apatite fission-track and zircon (U-Th)/He thermochronology. *Tectonophysics*, **649**, 47–57.

Sobczyk, A., Sobel, E.R. and Georgieva, V. 2019. Meso-Cenozoic cooling and exhumation history of the Orlica-Śnieżnik Dome (Sudetes, NE Bohemian Massif, Central Europe): Insights from apatite fission-track thermochronometry. *Terra Nova*, 2019, 1–12, doi. org/10.1111/ter.12449.

Stasiuk, L.D., Burgess, J., Thompson-Rizer, C., Hutton, A. and Cardott, B. 2002. Status report on TSOP-ICCP dispersed organic matter classification working group. *The Society for Organic Petrology Newsletter,* **19**, 1–14.

Suchý, V., Frey, M. and Wolf, M. 1997. Vitrinite reflectance and shear-induced graphitization in orogenic belts: A case study from the Kandersteg area, Helvetic Alps, Switzerland. *International Journal of Coal Geology*, **34**, 1–20.

Suchý, V., Sýkorová, I., Melka, K., Filip, J. and Machovič, V. 2007. Illite crystallinity, maturation of OM and microstructural development associated with lowest-grade metamorphism of Neoproterozoic sediments in the Teplá-Barrandian unit, Czech Republic. *Clay Minerals*, **42**, 415–438.

Suchý, V., Filip, J., Sýkorová, I., Pešek, J. and Kořínková, D. 2019. Palaeo-thermal and coalification history of Permo-Carboniferous sedimentary basins of Central and Western Bohemia, Czech Republic: first insights from apatite fission track analysis and vitrinite reflectance modelling. *Bulletin of Geosciences*, **94** (2), 201–219.

Sweeney, J.J. and Burnham, A.K. 1990. Evaluation of a simple model of vitrinite reflectance based on chemical kinetics. *AAPG Bulletin*, **74**, 1559–1570.

Taylor, G.H., Teichmüller, M., Davis, A., Diessel, C.F.K., Littke, R. and Robert, P. 1998. *Organic Petrology: A New Handbook Incorporating Some Revised Parts of Stach's Textbook of Coal Petrology*. 704 pp. Gebrüder Borntraeger; Berlin.

Teichmüller, M. 1982. Application of coal petrological methods in geology including oil and natural gas prospecting. In: Stach, E., Mackowsky, M.Th., Teichmüller, M., Taylor, G.H., Chandra, D. and Teichmüller, R. (eds), Stach's textbook of coal petrology, 381–413. Gebruder Borntraeger; Berlin.

Teichmüller, R. and Teichmüller, M. 1986. Relations between coalification and paleogeothermics in Variscan and Alpidic foredeeps of Western Europe. In: Buntebarth, G. and Stegena, L. (eds), Paleogeothermics: Lecture notes in Earth Sciences 5, 53–78, Springer-Verlag; New York.

Teichmüller, M., 1987. Organic material and very low-grade metamorphism. In: Frey, M. (ed.), Low-temperature metamorphism, 114–161, Chapman and Hall; New York.

Teisseyre, A.K. 1968. The Lower Carboniferous of the Intra-Sudetic Basin: Sedimentary petrology and basin analysis. *Geologia Sudetica*, **4**, 221–298.

Teisseyre, A.K. 1975. Sedimentology and Paleogeography of the Kulm alluvial fans in the western Intra-Sudetic Basin (Central Sudetes, SW Poland). *Geologia Sudetica*, **9**, 7–135.

Ting, F.T.C. 1978. Petrographic techniques in coal analysis. In: Karr, C. (Ed.), Analytical Methods for Coal and Coal Products, 3–26, Academic Press; New York.

Toboła, T. 2018. Raman spectroscopy of organic, solid and fluid inclusions in the Oldest Halite of LGOM area (SW Poland). *Spectrochimica Acta Part A: Molecular and Biomolecular Spectroscopy*, **189**, 381–392.

Todd, J. and Pickel, W. 2011. Comparison of Random and Maximum Reflectance Analysis. Results of Coal and Organic Petrology Services, Internal Report.

Tuinstra, F. and Koenig, J.L. 1970. Raman spectrum of graphite. *Journal of Chemistry and Physics*, **53**, 1126–1130.

Turnau, E., Żelaźniewicz, A. and Franke, W. 2005. Middle to early late Viséan onset of late orogenic sedimentation in the Intra-Sudetic Basin, West Sudetes: miospore evidence and tectonic implication. *Geologia Sudetica*, **34**, 9–16.

Uličný, D., Špičáková, L., Grygar, R., Svobodová, M., Čech, S., Laurin, J. 2009. Palaeodrainage systems at the basal unconformity of the Bohemian Cretaceous Basin: roles of inherited fault systems and basement lithology during the onset of basin filling. *Bulletin of Geosciences*, **84**, 577–610.

Uličný, D. 2001. Depositional systems and sequence stratigraphy of coarse-grained deltas in a shallow-marine, strike-slip setting: the Bohemian Cretaceous Basin, Czech Republic. *Sedimentology*, **48**, 599–628.

Ulrych, J., Dostal, J., Adamovič, J., Jelínek, E., Špaček, P.,

Hegner, E. and Balogh, K. 2011. Recurrent Cenozoic volcanic activity in the Bohemian Massif (Czech Republic). *Lithos*, **123**, 133–144.

Ulrych, J., Fediuk, F., Lang, M. and Martinec, P. 2004. Late Paleozoic volcanic rocks of the Intra-Sudetic Basin, Bohemian Massif: petrological and geochemical characteristics. *Chemie der Erde – Geochemistry*, **64**, 127–153.

Ulrych, J., Pešek, J., Štěpánková-Svobodova, J., Bosák, P., Lloyd, F.E., von Seckendorff, V., Lang, M. and Novák, J.K. 2006. Permo-Carboniferous volcanism in late Variscan continental basins of the Bohemian Massif (Czech Republic): geochemical characteristic. *Chemie der Erde – Geochemistry*, **66**, 37–56.

Ulyanova, E.V., Molchanov, A.N., Prokhorov, I.Y. and Grinyov, V. G. 2014. Fine structure of Raman spectra in coals of different rank. *International Journal of Coal Geology*, **121**, 37–43.

Ventura, B., Lisker, F. and Kopp, J. 2009. Thermal and denudation history of the Lusatian Block (NE Bohemian Massif, Germany) as indicated by apatite fission-track data. In: Lisker, F., Ventura, B. and Glasmacher, U.A. (eds.), Thermochronological methods: from Palaeotemperature constraints to landscape evolution models. *Geological Society, London, Special Publications*, **324**, 181–192.

Waliczek, M., Machowski, G., Więcław, D., Konon, A., Wandycz, P. 2019. Properties of solid bitumen and other organic matter from Oligocene shales of the Fore-Magura Unit in Polish Outer Carpathians: Microscopic and geochemical approach. *International Journal of Coal Geology*, **210**, No 103206, https://doi.org/10.1016/j.coal.2019.05.013.

Wilkins, R.W.T., Boudou, R., Sherwood, N. and Xiao, X. 2014. Thermal maturity evaluation of inertinites by Raman spectroscopy: the RaMM technique. *International Journal of Coal Geology*, **128-129**, 143–152.

Wilkins, R.W.T., Wang, M., Gan, H. and Li, Z. 2015. A RaMM study of thermal maturity of dispersed organic matter in marine source rocks. *International Journal of Coal Geology*, **150-151**, 252–264.

Wojewoda, J., Rauch, M. and Kowalski, A. 2016. Synsedimentary seismotectonic features in Triassic and Cretaceous sediments of the Intra-Sudetic Basin (U Devìti Krížù locality) – regional implications. *Geological Quarterly,* **60**, 355–364.

Wopenka, B. and Pasteris, J.D. 1993. Structural characterization of kerogens to granulite-facies graphite: Applicability of Raman microprobe spectroscopy. *American Mineralogist*, **78**, 533–557.

Żakowa, H. 1963. Stratigraphy and facial extents of the Lower Carboniferous in the Sudetes. *Kwartalnik Geologiczny*, **7**, 73–94 [in Polish with English summary].

Zhang, Y. and Li, Z. 2019. Raman spectroscopic study of chemical structure and thermal maturity of vitrinite from a suite of Australia coals. *Fuel*, **241**, 188–198.

Ziegler, P.A. 1987. Late Cretaceous and Cainozoic intraplate compressional deformations in the Alpine foreland. *Tectonophysics*, **137**, 389–420.

Ziegler, P.A., Bertotti, G. and Cloetingh, S.A.P.L. 2002. Dynamic processes controlling foreland development: the role of mechanical (de)coupling of orogenic wedges and forelands. In: Bertotti, G., Schulmann, K. and Cloetingh, S.A.P.L. (Eds), Continental Collision and the tectono-sedimentary evolution of forelands. *Stephan Mueller Special Publication Series*, **1**, 17–56.

Ziegler, P.A. and Dèzes, P. 2007. Cenozoic uplift of Variscan Massifs in the Alpine foreland: Timing and controlling mechanisms. *Global and Planetary Change*, **58**, 237–269.

Manuscript submitted: 6th July 2019
Revised version accepted: 28th January 2020